

ANALYSIS AND NUMERICAL SIMULATION OF MAGNETIC FORCES BETWEEN RIGID POLYGONAL BODIES. PART II: NUMERICAL SIMULATION

NIKOLA POPOVIĆ, DIRK PRAETORIUS, AND ANJA SCHLÖMERKEMPER

ABSTRACT. The analysis of magnetoelastic phenomena is a field of active research. Formulae for the magnetic force in macroscopic systems have been under discussion for some time. In [PPS], we rigorously justify several of the available formulae in the context of rigid bodies in two and three space dimensions. In the present, second part of our study, we investigate these formulae in a series of numerical experiments in which the magnetic force is computed in dependence on the geometries of the bodies as well as on the distance between them. In case the two bodies are in contact, i.e., in the limit as their distance tends to zero, we focus especially on a formula obtained in a discrete-to-continuum approximation. The aim of our study is to help clarify the question which force formula is the correct one in the sense that it describes nature most accurately and to suggest adequate real-life experiments for a comparison with the provided numerical data.

1. INTRODUCTION

The analysis of magnetoelastic phenomena is a field of active research. In particular, the question which formula most appropriately describes the magnetic force in macroscopic magnetized systems has been under investigation for quite some time. The controversy concerns formulae for the force within a magnetic body (i.e., the force exerted by one portion of such a body on its “nested” complement) as well as for the case of two magnetic bodies that are in contact, but not necessarily nested. For details on the various force formulae that have been considered in the literature, we refer the reader to [Bro66, DPG96, EM90] and the references therein; a recent clarifying exposition can be found in [Bob00].

The present article is the continuation of a study commenced in [PPS]. There, we discuss several of the formulae which have been proposed to describe the magnetic force in the context of rigid magnetized bodies in two and three space dimensions. We give a rigorous analytical justification of these formulae under quite general assumptions on the regularity of the respective domains and on the magnetizations. For the convenience of the reader, we recall the assumptions from [PPS] that are relevant here: Given $A, B \subset \mathbb{R}^d$ with $d = 2$ or $d = 3$ fixed, we assume that A and B are bounded Lipschitz domains with polygonal boundaries and finitely many corners or edges. Moreover, the corresponding magnetization fields $\mathbf{m}_A : A \rightarrow \mathbb{R}^d$ and $\mathbf{m}_B : B \rightarrow \mathbb{R}^d$ are Lipschitz continuous, and are supported on \bar{A} and \bar{B} , respectively, i.e., there holds $\mathbf{m}_A \in W^{1,\infty}(A)$ and $\mathbf{m}_B \in W^{1,\infty}(B)$. (Here, the bars denote closure with respect to the usual Euclidean norm on \mathbb{R}^d .)

The analysis in [PPS] proceeds as follows: In case the two bodies are separated, i.e., if the distance between A and B is greater than zero, we focus on a well-known classical force formula, see e.g. [Bob00, Bro66], which we denote by \mathbf{F} . If A and B are in contact, i.e., if the distance between the two bodies is zero, we state and rigorously prove two different formulae for the force: One of these, \mathbf{F}^{Br} , is a formula which was first introduced by Brown [Bro66]; the other formula, \mathbf{F}^{lim} , is derived in a discrete-to-continuum limit and was first considered in [Sch02, Sch05] in the

Date: March 3, 2011.

Key words and phrases. Magnetostatics, magnetic force formulae, numerical simulation, single-layer potential.
2006 *PACS.* 41.20.Gz, 45.20.da, 02.60.Cb.

context of three-dimensional nested magnetic bodies. The relevant analytical results for the present work can be found in [PPS, Theorem 3.1] respectively in [PPS, Theorems 3.3 and 3.4].

The aim of this second part of our study is to illustrate and compare the three formulae \mathbf{F} , \mathbf{F}^{Br} , and \mathbf{F}^{lim} discussed in [PPS] in a series of numerical experiments. To that end, we restrict ourselves to the simplified setting of uniformly magnetized polygonal domains in two and three dimensions, i.e., we only consider rectangular and cuboidal magnetic bodies, respectively, on which the magnetization is assumed to be constant. (To state it in physical terms, we focus on hard permanent magnets.) This simplification has the advantage that all integrals occurring in the implementation of the above force formulae can be evaluated analytically. In Section 2, we outline how the resulting analytical expressions can be implemented algorithmically. More specifically, it turns out that the implementation reduces to the computation of certain double boundary integrals over affine boundary pieces or two-dimensional screens, respectively: For $d = 2$, these integrals are of the type of the so-called single-layer potential and are hence readily computable, see e.g. [Mai99, Pra03]; for $d = 3$, the evaluation of the corresponding integrals requires the evaluation of rather involved antiderivatives which can, however, be recursively reduced to more elementary ones [Mai00].

In Section 3, we report on the results of our numerical experiments. These experiments are set up as follows: For either $d = 2$ or $d = 3$ fixed, we define the two bodies A and B in dependence on some geometry parameter $L > 0$ which denotes the length, height, or width of one or both of the bodies. First, we consider the force in case the two bodies are a positive distance ε apart; more precisely, we introduce a shifted copy B_ε of B , with $B_0 = B$, and we compute the force acting between A and B_ε according to the classical formula \mathbf{F} . In particular, we study the dependence of the force on the parameters ε and L , where the focus is primarily on ε small.

Moreover, if the distance between A and B_ε is zero, we additionally compute the magnetic force according to the formulae \mathbf{F}^{Br} and \mathbf{F}^{lim} obtained in that case. This last aspect is closely related to our principal objective and provides the physical motivation for our study: In Section 4, we interpret our numerical results comparatively, and we discuss them in view of corresponding real-life experiments. Finally, we summarize open problems and suggestions for future work.

2. IMPLEMENTATION

In this section, we show how the analytical results of [PPS] can be implemented numerically; in particular, it turns out that under the assumptions of [PPS], the integrals occurring in the implementation can be evaluated analytically if we additionally require that the magnetizations are constant.

Recall that for constant magnetization fields \mathbf{m}_A and \mathbf{m}_B and $\text{dist}(A, B) > 0$, we have

$$(2.1) \quad \mathbf{F}_{\text{const}}(A, B) = -\gamma \int_{\partial A} (\mathbf{m}_A \cdot \mathbf{n}_A)(x) \int_{\partial B} (\mathbf{m}_B \cdot \mathbf{n}_B)(y) \nabla N(x - y) ds_y ds_x,$$

cf. [PPS, Equation (2.4)], whereas for $\text{dist}(A, B) = 0$, there holds

$$(2.2) \quad \begin{aligned} \mathbf{F}_{\text{const}}^{\text{Br}}(A, B) &= -\gamma \int_{\partial A} (\mathbf{m}_A \cdot \mathbf{n}_A)(x) \oint_{\partial B} (\mathbf{m}_B \cdot \mathbf{n}_B)(y) \nabla N(x - y) ds_y ds_x \\ &\quad + \frac{\gamma}{2} \int_{\partial A \cap \partial B} (\mathbf{m}_A \cdot \mathbf{n}_A)(\mathbf{m}_B \cdot \mathbf{n}_A) \mathbf{n}_A ds_x, \end{aligned}$$

$$(2.3) \quad \mathbf{F}_{\text{const}}^{\text{long}}(A, B) = \mathbf{F}_{\text{const}}^{\text{Br}}(A, B) - \frac{\gamma}{2} \int_{\partial A \cap \partial B} (\mathbf{m}_A \cdot \mathbf{n}_A)(\mathbf{m}_B \cdot \mathbf{n}_A) \mathbf{n}_A ds_x,$$

$$(2.4) \quad \mathbf{F}_{\text{const}}^{\text{lim}}(A, B) = \mathbf{F}_{\text{const}}^{\text{long}}(A, B) + \frac{1}{2} \sum_{i,j,p=1}^d (S_{ij1p}, \dots, S_{ijd p}) \int_{\partial A \cap \partial B} (\mathbf{m}_A)_i (\mathbf{m}_B)_j (\mathbf{n}_A)_p ds_x,$$

see [PPS, Equations (3.8), (3.20), and (3.28)], respectively. Here, N denotes the Newtonian kernel, cf. [PPS, Section 2], and $\oint_{\partial B}(\cdot) ds_y$ stands for the Cauchy principal value integral. Moreover, S_{ijkp} , $i, j, k, p = 1, \dots, d$, are real numbers determined by a singular lattice sum which only depends on the underlying Bravais lattice \mathcal{L} , see [PPS, Equation (3.22)] for details. The constant factor γ , which depends on the choice of physical units [PPS], shows up in every term in the above formulae; without loss of generality, we will therefore set $\gamma = 1$ in the following. (Recall that this choice of γ corresponds to the Gaussian unit system.)

Since \mathbf{m}_A and \mathbf{m}_B are constant on the polygonal domains A and B , respectively, it follows that $\mathbf{m}_A \cdot \mathbf{n}_A$ and $\mathbf{m}_B \cdot \mathbf{n}_B$ are piecewise constant on ∂A and ∂B . Hence, from an implementational point of view, the main task is the computation of integrals of the form

$$(2.5) \quad - \int_E \oint_{\tilde{E}} \nabla N(x-y) ds_y ds_x = \frac{1}{|\mathbb{S}^{d-1}|} \int_E \oint_{\tilde{E}} \frac{x-y}{|x-y|^d} ds_y ds_x,$$

where E, \tilde{E} are affine boundary pieces for $d = 2$ and two-dimensional screens for $d = 3$, respectively. Moreover, \mathbb{S}^{d-1} and $|\mathbb{S}^{d-1}|$ denote the unit sphere in \mathbb{R}^d and its surface measure, respectively.

Analytical formulae for integrals of the type (2.5) are known from the numerical discretization of boundary integral equations by Galerkin schemes with piecewise constant ansatz and test functions. All integrals arising in our implementation will be evaluated exactly using such formulae. We note that for any unitary transformation Q , there holds

$$(2.6) \quad \begin{aligned} \int_E \oint_{\tilde{E}} \frac{x-y}{|x-y|^d} ds_y ds_x &= \int_{Q^{-1}(E)} \oint_{Q^{-1}(\tilde{E})} \frac{Q(x-y)}{|Q(x-y)|^d} ds_y ds_x \\ &= Q \int_{Q^{-1}(E)} \oint_{Q^{-1}(\tilde{E})} \frac{x-y}{|x-y|^d} ds_y ds_x \end{aligned}$$

in (2.5), which will be exploited in the following to simplify the implementation considerably.

2.1. The Two-Dimensional Case. First, we outline how (2.5) can be implemented when $d = 2$. For ease of presentation, we restrict ourselves to the cases when E and \tilde{E} are either parallel or perpendicular, respectively. While it turns out that for $d = 2$, explicit formulae can be obtained for arbitrary affine boundary pieces E and \tilde{E} [Mai99, Pra03], the above two cases are the only ones that will occur in the numerical experiments below, cf. Section 3.

In order to derive closed-form formulae for (2.5) in the present setting, we define the antiderivatives

$$(2.7) \quad \mathcal{S}(x_1; y_1, x_2 - y_2) := \int \log|x-y| dx_1,$$

$$(2.8) \quad \mathcal{F}(x_1, y_1; x_2 - y_2) := (x_2 - y_2) \iint \frac{1}{|x-y|^2} dy_1 dx_1.$$

Here, variables before the semicolon indicate integration variables, whereas variables after the semicolon are constant with respect to the integration. This notation will be useful for the analytical computation of the above integrals. Note that the integral in (2.7) is of the type of the so-called single-layer potential and, hence, that it can be computed using the formulae found e.g. in [Mai99] or in [Pra03]. The relevant results are summarized in Appendix A.1.

Remark 2.1. Here and in the following, the term antiderivative is to be understood as follows: We write

$$F(x) = \int \dots \int f(x_1, \dots, x_n) dx_n \dots dx_1 \quad \text{in } \Omega \subset \mathbb{R}^n$$

in abbreviation of

$$\frac{\partial}{\partial x_n} \dots \frac{\partial}{\partial x_1} F(x) = f(x) \quad \text{for all } x \in \Omega.$$

For instance, given $\Omega = [a_1, b_1] \times [c_2, d_2] \subset \mathbb{R}^2$ and $F(x) = \iint f(x_1, x_2) dx_2 dx_1$, the integral of f over Ω can be computed via

$$\int_{\Omega} f(x) dx = \int_{a_1}^{b_1} \int_{c_2}^{d_2} \frac{\partial}{\partial x_2} \frac{\partial}{\partial x_1} F(x_1, x_2) dx_2 dx_1 = F(b_1, d_2) - F(b_1, c_2) - F(a_1, d_2) + F(a_1, c_2).$$

□

Case 1_{2D} (E, \tilde{E} parallel): After applying an appropriately defined rotation Q in (2.6), we may assume without loss of generality that the 2-direction is constant, i.e., that

$$(2.9) \quad E = [a_1, b_1] \times \{x_2\} \quad \text{and} \quad \tilde{E} = [c_1, d_1] \times \{y_2\}$$

holds with scalars $a_1, b_1, c_1, d_1, x_2, y_2 \in \mathbb{R}$.

Observation 1. For $\text{dist}(E, \tilde{E}) > 0$, (2.5) exists as a classical Riemann integral instead of as a Cauchy principal value integral. □

When $\text{dist}(E, \tilde{E}) = 0$, several possibilities have to be accounted for: E and \tilde{E} may be equal, or else $E \cap \tilde{E}$ may be an affine boundary piece or even just a single point.

Observation 2. For $E = \tilde{E}$, (2.5) vanishes. This can be seen as follows: Define $a = (a_1, x_2)$ and $b = (b_1, x_2)$, respectively, and let $[a, b] = \text{conv}\{a, b\}$. Then, following [Pra03, Satz A.2], we have that for $x \in (a, b)$,

$$(2.10) \quad \begin{aligned} \oint_E \frac{x-y}{|x-y|^2} ds_y &= \lim_{\varepsilon \rightarrow 0} \left(\int_{[(a_1, x_2), (x_1 - \varepsilon, x_2)]} \frac{x-y}{|x-y|^2} ds_y + \int_{[(x_1 + \varepsilon, x_2), (b_1, x_2)]} \frac{x-y}{|x-y|^2} ds_y \right) \\ &= -(\text{sgn}(b_1 - a_1), 0)^T \lim_{\varepsilon \rightarrow 0} \left(\log \frac{\varepsilon}{|a_1 - x_1|} + \log \frac{|b_1 - x_1|}{\varepsilon} \right) \\ &= -\frac{b_1 - a_1}{|b_1 - a_1|} (1, 0)^T \log \frac{|b_1 - x_1|}{|a_1 - x_1|} = -\frac{b-a}{|b-a|} \log \frac{|b-x|}{|a-x|}. \end{aligned}$$

Here we have used $\text{sgn}(x_1 - \varepsilon - a_1) = \text{sgn}(b_1 - a_1) = \text{sgn}(b_1 - x_1 - \varepsilon)$ for ε sufficiently small and the fact that the ε -dependent terms in (2.10) cancel. Now, given that surface integrals are independent of their parametrization, we obtain with $x = a + t(b-a) \in \mathbb{R}^2$, $t \in (0, 1)$ and $x = b + t'(a-b) \in \mathbb{R}^2$, $t' \in (0, 1)$, respectively, that

$$(2.11) \quad \begin{aligned} \int_{[a,b]} \log \frac{|b-x|}{|a-x|} ds_x &= \int_{[a,b]} \log |b-x| ds_x - \int_{[a,b]} \log |a-x| ds_x \\ &= |b-a| \left(\int_0^1 \log |(b-a)(1-t)| dt - \int_0^1 \log |(a-b)(1-t')| dt' \right) = 0. \end{aligned}$$

□

Next, assume that $\text{dist}(E, \tilde{E}) = 0$ in (2.5), but that $E \neq \tilde{E}$. One possibility is for E and \tilde{E} to have one of their end points in common:

Observation 3. For $E \cap \tilde{E} = \{z\}$, with z equal to either $a = (a_1, x_2)$, $b = (b_1, x_2)$, $c = (c_1, y_2)$, or $d = (d_1, y_2)$, (2.5) exists as an improper integral. In particular, assuming e.g. $b = c$, we have

$$(2.12) \quad \int_E \oint_{\tilde{E}} \frac{x-y}{|x-y|^2} ds_y ds_x = -2 \frac{b-d}{|b-d|} \left((b_1 - d_1) \log \frac{|b-d|}{|b-a|} - (a_1 - d_1) \log \frac{|a-d|}{|b-a|} \right).$$

We first consider (2.5) with \tilde{E} replaced by $\tilde{E}_\varepsilon = [b_1 + \varepsilon, d_1] \times \{x_2\}$ and then take the limit as $\varepsilon \rightarrow 0$; note that clearly $x_2 = y_2$. For the inner integral, there holds

$$\int_{\tilde{E}_\varepsilon} \frac{x-y}{|x-y|^2} ds_y = -(\operatorname{sgn}(d_1 - b_1 - \varepsilon), 0)^T \log \frac{|d_1 - x_1|}{|b_1 + \varepsilon - x_1|}$$

as in (2.10), cf. again [Pra03, Satz A.2]. Now,

$$(2.13) \quad \int_E \oint_{\tilde{E}_\varepsilon} \frac{x-y}{|x-y|^2} ds_y ds_x = -\frac{d-b-(\varepsilon, 0)^T}{|d-b-(\varepsilon, 0)^T|} \left(\int_{[a,b]} \log |d-x| ds_x - \int_{[a,b]} \log |b+(\varepsilon, 0)^T-x| ds_x \right),$$

which is again of single-layer type. Thus, (2.13) can be evaluated analytically: Following [Pra03, Satz A.4], we obtain

$$(2.14) \quad \int_{[a,b]} \log |d-x| ds_x = 2 \left(|b_1 - a_1| (\log |b_1 - a_1| - 1) + (b_1 - d_1) \operatorname{sgn}(b_1 - a_1) \log \frac{|b_1 - d_1|}{|b_1 - a_1|} - (a_1 - d_1) \operatorname{sgn}(b_1 - a_1) \log \frac{|a_1 - d_1|}{|b_1 - a_1|} \right)$$

and

$$(2.15) \quad \int_{[a,b]} \log |b+\varepsilon-x| ds_x = 2 \left(|b_1 - a_1| (\log |b_1 - a_1| - 1) - \varepsilon \operatorname{sgn}(b_1 - a_1) \log \frac{\varepsilon}{|b_1 - a_1|} - (a_1 - b_1 - \varepsilon) \operatorname{sgn}(b_1 - a_1) \log \frac{|a_1 - b_1 - \varepsilon|}{|b_1 - a_1|} \right).$$

Since the terms in (2.15) involving ε vanish for $\varepsilon \rightarrow 0$, (2.12) follows. \square

Remark 2.2. Note that the above argument cannot be applied to show that (2.12) exists as an improper integral instead of just as a Cauchy principal value integral when $E = \tilde{E}$, since

$$\begin{aligned} \lim_{\substack{\delta \rightarrow 0 \\ \varepsilon \rightarrow 0}} \left(\int_{[(a_1, x_2), (x_1 - \delta, x_2)]} \frac{x-y}{|x-y|^2} ds_y + \int_{[(x_1 + \varepsilon, x_2), (b_1, x_2)]} \frac{x-y}{|x-y|^2} ds_y \right) \\ = -(\operatorname{sgn}(b_1 - a_1), 0)^T \lim_{\substack{\delta \rightarrow 0 \\ \varepsilon \rightarrow 0}} \left(\log \frac{\delta}{|a_1 - x_1|} + \log \frac{|b_1 - x_1|}{\varepsilon} \right) \end{aligned}$$

diverges. \square

Observation 4. The case of $|E \cap \tilde{E}| > 0$, i.e., the case when E and \tilde{E} overlap on a set of non-zero measure, is a linear combination of the previous cases. \square

Given Observations 1–4, we can derive a closed-form formula for (2.5) as follows. Without loss of generality, we may assume that E and \tilde{E} are either separated or that they have only a point in common. Thus, we need to evaluate the antiderivatives

$$(2.16) \quad D_j^{\parallel}(x_1, y_1; x_2 - y_2) := \int \int \frac{x_j - y_j}{|x - y|^2} dy_1 dx_1$$

for $j = 1, 2$. These can be expressed in terms of the antiderivatives \mathcal{S} and \mathcal{F} defined in (2.7) and (2.8), respectively. In particular, since Fubini's Theorem is applicable, we can change the order of integration in (2.16) at will. To that end, note that obviously

$$(2.17) \quad \frac{\partial}{\partial x_j} \log |x - y| = \frac{x_j - y_j}{|x - y|^2} = -\frac{\partial}{\partial y_j} \log |x - y|.$$

Then, D_1^\parallel is given by

$$\begin{aligned} D_1^\parallel &= \int \int \frac{x_1 - y_1}{|x - y|^2} dy_1 dx_1 = - \int \int \frac{\partial}{\partial y_1} \log |x - y| dy_1 dx_1 = - \int \log |x - y| dx_1 \\ &= -\mathcal{S}(x_1; y_1, x_2 - y_2). \end{aligned}$$

For D_2^\parallel , we obtain

$$D_2^\parallel = (x_2 - y_2) \int \int \frac{1}{|x - y|^2} dy_1 dx_1 = \mathcal{F}(x_1, y_1; x_2 - y_2),$$

which is trivially zero for $x_2 = y_2$ and which can be integrated directly otherwise, see Appendix A.1.

Observation 5. With $a, b, c, d \in \mathbb{R}^2$,

$$\mathcal{I}(E, \tilde{E}) = \int_{[a,b]} \oint_{[c,d]} \frac{x - y}{|x - y|^2} ds_y ds_x,$$

and E and \tilde{E} defined as in (2.9), there holds without any further assumption

$$(2.18) \quad \mathcal{I}_1(E, \tilde{E}) = \int_{a_1}^{b_1} \log |x - d| dx_1 - \int_{a_1}^{b_1} \log |x - c| dx_1$$

and

$$(2.19) \quad \mathcal{I}_2(E, \tilde{E}) = (x_2 - y_2) \int_{a_1}^{b_1} \int_{c_1}^{d_1} \frac{1}{|x - y|^2} dy_1 dx_1.$$

The assertion of Observation 5 can be seen as follows: If E, \tilde{E} are “regular,” i.e., if they are either separated or overlap only on a set of measure zero, the result follows from the preceding Observations. Now, assume that E and \tilde{E} overlap on a set of non-zero measure; without loss of generality, we only consider the particular case $[c, d] \subseteq [a, b]$. Then, introducing an obvious short-hand notation, we can write

$$\int_{[a,b]} \oint_{[c,d]} = \int_{[a,c]} \oint_{[c,d]} + \int_{[c,d]} \oint_{[c,d]} + \int_{[d,b]} \oint_{[c,d]},$$

where the second term is zero by Observation 2 and the Cauchy principal value integrals in the first and third term are just regular integrals (in the sense of Observation 3). Hence, they can be evaluated using the formulae derived for $|E \cap \tilde{E}| = 0$ above. This concludes the argument. \square

In sum, it follows that to evaluate (2.9) for any choice of E and \tilde{E} , one only has to compute the antiderivatives \mathcal{I}_1 and \mathcal{I}_2 defined in (2.18) and (2.19), respectively. To state it differently, for the implementation only the regular case has to be considered.

Case 2_{2D} (E, \tilde{E} perpendicular): As in Case 1_{2D}, it is no restriction to assume that E and \tilde{E} are defined by

$$(2.20) \quad E = [a_1, b_1] \times \{x_2\} \quad \text{and} \quad \tilde{E} = \{y_1\} \times [c_2, d_2].$$

An argument similar to the one given in Observation 3 above can be applied to show that for E, \tilde{E} perpendicular, (2.5) exists as an improper integral when E and \tilde{E} have one point in common. Therefore, it remains to compute the antiderivatives

$$(2.21) \quad D_j^\perp(x_1, y_2; x_2, y_1) := \int \int \frac{x_j - y_j}{|x - y|^2} dy_2 dx_1$$

for $j = 1, 2$. In particular, given (2.17), we have

$$D_1^\perp := \int \log |x - y| dy_2 = \mathcal{S}(y_2; x_2, x_1 - y_1)$$

for $j = 1$ and

$$D_2^\perp := - \int \log |x - y| dx_1 = -\mathcal{S}(x_1; y_1, x_2 - y_2)$$

for $j = 2$, respectively.

2.2. The Three-Dimensional Case. We now indicate how (2.5) can be implemented for $d = 3$. To the best of our knowledge, no analytical formulae are available for arbitrary screens E, \tilde{E} in three-dimensional space. However, for the numerical experiments in Section 3 below, it suffices to consider the case where E and \tilde{E} are axis-oriented rectangular screens which are either parallel or perpendicular to the coordinate axes. In that case, (2.5) can in fact be computed analytically.

For the derivation of closed-form formulae for (2.5), we define the following antiderivatives which can be found in [Mai00]:

$$(2.22) \quad F_{k\ell mn}^p(x_1, x_2, y_1, y_2; x_3 - y_3) := \int \int \int \int x_1^k x_2^\ell y_1^m y_2^n |x - y|^{2p} dy_2 dy_1 dx_2 dx_1,$$

$$(2.23) \quad G_{k\ell m}^p(y_1, y_2, y_3; x_1, x_2, x_3) := \int \int \int y_1^k y_2^\ell y_3^m |x - y|^{2p} dy_3 dy_2 dy_1,$$

$$(2.24) \quad \mathcal{G}_{\ell mn}^p(x_2, y_1, y_2; x_1, x_3 - y_3) := \int \int \int x_2^\ell y_1^m y_2^n |x - y|^{2p} dy_2 dy_1 dx_2.$$

We will only consider (2.22)–(2.24) for $k = \ell = m = n = 0$ and $p = -\frac{3}{2}, -\frac{1}{2}$, respectively. The corresponding formulae from [Mai00] are summarized in Appendix A.2. For the convenience of the reader, we retain the notation of [Mai00] throughout.

Case 1_{3D} (E, \tilde{E} parallel): After applying a rotation if necessary, we may assume without loss of generality that the 3-direction in (2.5) is constant, i.e., that E and \tilde{E} are given by

$$(2.25) \quad E = [a_1, b_1] \times [a_2, b_2] \times \{x_3\} \quad \text{and} \quad \tilde{E} = [c_1, d_1] \times [c_2, d_2] \times \{y_3\}$$

with scalars $a_j, b_j, c_j, d_j, x_3, y_3 \in \mathbb{R}$. Hence, we are concerned with the computation of the anti-derivative

$$(2.26) \quad D_j^\parallel(x_1, x_2, y_1, y_2; x_3 - y_3) := \int \int \int \int \frac{x_j - y_j}{|x - y|^3} dy_2 dy_1 dx_2 dx_1.$$

As in the two-dimensional case, we first collect a few observations:

Observation 1. For $\text{dist}(E, \tilde{E}) > 0$, the existence of the double boundary integrals in (2.5) is obvious. \square

Observation 2. When $\text{dist}(E, \tilde{E}) = 0$ and $E = \tilde{E}$, a symmetry argument similar to the one given in Case 1_{2D} above can be applied to show that (2.5) vanishes. \square

Observation 3. The formulae given below are valid even when $\text{dist}(E, \tilde{E}) = 0$ as long as $|E \cap \tilde{E}| = 0$, since (2.5) then still exists as an improper integral (rather than just as a Cauchy principal value integral), see our discussion of the two-dimensional case.

We will outline the proof for the case when E and \tilde{E} have only one edge in common; without loss of generality, we assume $b_1 = c_1$, $[a_2, b_2] = [c_2, d_2]$, and $x_3 = y_3$ in (2.25). Then, by Fubini's

Theorem, it suffices to show that the corresponding improper integral of $|\nabla N(x - y)|$ exists. For $\varepsilon > 0$ small and $\tilde{E}_\varepsilon = [b_1 + \varepsilon, d_1] \times [a_2, b_2] \times \{x_3\}$, it follows that

$$\begin{aligned}
(2.27) \quad & \int_E \int_{\tilde{E}_\varepsilon} |\nabla N(x - y)| ds_y ds_x \\
& := \int_{[a_1, b_1]} \int_{[a_2, b_2]} \int_{[b_1 + \varepsilon, d_1]} \int_{[a_2, b_2]} \frac{1}{(x_1 - y_1)^2 + (x_2 - y_2)^2} dy_2 dy_1 dx_2 dx_1 \\
& = \int_{a_1}^{b_1} \int_{a_2}^{b_2} \int_{x_1 - b_1 - \varepsilon}^{x_1 - d_1} \int_{x_2 - a_2}^{x_2 - b_2} \frac{1}{u^2 + v^2} dv du dx_2 dx_1 \\
& = \int_{a_1}^{b_1} \int_{a_2}^{b_2} \int_{x_1 - b_1 - \varepsilon}^{x_1 - d_1} \frac{1}{u} \arctan \frac{v}{u} \Big|_{v=x_2 - a_2}^{x_2 - b_2} du dx_2 dx_1.
\end{aligned}$$

Taking into account that the arctangent is bounded by $\frac{\pi}{2}$ and integrating out u and x_2 , we see that

$$\int_E \int_{\tilde{E}_\varepsilon} |\nabla N(x - y)| ds_y ds_x \lesssim \int_{a_1}^{b_1} \log \frac{|x_1 - d_1|}{|x_1 - b_1 - \varepsilon|} dx_1$$

up to a multiplicative constant. The right-hand side converges for $\varepsilon \rightarrow 0$, cf. (2.13). Hence, the existence of (2.5) follows from the Dominated Convergence Theorem.

Note that similar considerations apply when E and \tilde{E} have just one point in common. \square

Observation 4. The more general case of $|E \cap \tilde{E}| > 0$ can again be treated as a linear combination of the previous cases. \square

Provided that the parallel screens E and \tilde{E} are either separated or that they have only an edge or a point in common (i.e., that they overlap only on a set of measure zero), the prerequisites for applying Fubini's Theorem hold, and we can choose an arbitrary order of integration as long as the final result is finite. We will make use of the following simple relation:

$$(2.28) \quad -\frac{\partial}{\partial x_j} \frac{1}{|x - y|} = \frac{x_j - y_j}{|x - y|^3} = \frac{\partial}{\partial y_j} \frac{1}{|x - y|}.$$

For D_1^\parallel , we obtain

$$\begin{aligned}
D_1^\parallel &= - \int \int \int \int \frac{\partial}{\partial x_1} \frac{1}{|x - y|} dx_1 dy_2 dy_1 dx_2 = - \int \int \int \frac{1}{|x - y|} dy_2 dy_1 dx_2 \\
&= -\mathcal{G}_{000}^{-1/2}(x_2, y_1, y_2; x_1, x_3 - y_3).
\end{aligned}$$

For the second component of (2.5), one can write in an analogous manner

$$D_2^\parallel = - \int \int \int \frac{1}{|x - y|} dy_2 dy_1 dx_1 = -\mathcal{G}_{000}^{-1/2}(x_1, y_2, y_1; x_2, x_3 - y_3).$$

The computation of D_3^\parallel is different in that we are not led to $\mathcal{G}_{000}^{-1/2}$ now, but to $F_{0000}^{-3/2}$:

$$D_3^\parallel = (x_3 - y_3) \int \int \int \int \frac{1}{|x - y|^3} dy_2 dy_1 dx_2 dx_1 = (x_3 - y_3) F_{0000}^{-3/2}(x_1, x_2, y_1, y_2; x_3 - y_3).$$

Observation 5. By similar arguments as in the two-dimensional case, it follows that only the regular case of $|E \cap \tilde{E}| = 0$ has to be implemented, cf. Observation 5 above. \square

Case 2_{3D} (E, \tilde{E} perpendicular): According to (2.6), we may assume without loss of generality that there exist scalars $a_j, b_j, c_j, d_j, x_3, y_1 \in \mathbb{R}$ with

$$(2.29) \quad E = [a_1, b_1] \times [a_2, b_2] \times \{x_3\} \quad \text{and} \quad \tilde{E} = \{y_1\} \times [c_2, d_2] \times [c_3, d_3].$$

Arguments similar to the ones given in Case 1_{3D} above can be applied to prove that the Cauchy principal value integral in (2.5) exists as an improper integral. The proofs then reduce to the corresponding convergence results for E, \tilde{E} perpendicular in two dimensions.

In sum, the implementation of (2.5) thus recurs to the computation of the antiderivatives

$$(2.30) \quad D_j^\perp(x_1, x_2, y_2, y_3; x_3, y_1) := \int \int \int \int \frac{x_j - y_j}{|x - y|^3} dy_3 dy_2 dx_2 dx_1.$$

In particular, for $j = 1$ we obtain

$$D_1^\perp = - \int \int \int \frac{1}{|x - y|} dy_3 dy_2 dx_2 = -\mathcal{G}_{000}^{-1/2}(x_2, y_3, y_2; x_3, x_1 - y_1);$$

the second component reads

$$D_2^\perp = - \int \int \int \frac{1}{|x - y|} dy_3 dy_2 dx_1 = -\mathcal{G}_{000}^{-1/2}(x_1, y_2, y_3; y_1, x_2, x_3);$$

finally, for $j = 3$ we find

$$D_3^\perp = \int \int \int \frac{1}{|x - y|} dy_2 dx_2 dx_1 = \mathcal{G}_{000}^{-1/2}(y_2, x_1, x_2; y_1, y_3 - x_3).$$

3. NUMERICAL EXPERIMENTS

In this section, we present a series of numerical experiments, both in two and in three dimensions, to illustrate and compare the formulae \mathbf{F} , \mathbf{F}^{Br} , and \mathbf{F}^{lim} discussed in [PPS, Sections 2 and 3], see also (2.1), (2.2), and (2.4). (Here, we again assume $\gamma = 1$ throughout.) We have implemented several model cases, with A and B rectangular or cuboidal and of varying length, height, or depth L , respectively. Moreover, following Section 2, we take the magnetization fields \mathbf{m}_A and \mathbf{m}_B to be constant. An overview of all experiments discussed in the subsections below is provided in Table 3.1.

First, we consider the force formula (2.1) for separated bodies. For convenience, we introduce the following notation: Let A and B_ε be two bodies that are a distance $\varepsilon > 0$ apart, and whose geometries depend on some parameter $L > 0$. Then, we write

$$\mathbf{F}(\varepsilon, L) := \mathbf{F}_{\text{const}}(A, B_\varepsilon).$$

Additionally, for $\varepsilon = 0$, i.e., for two bodies A and B in contact, the contributions coming from Brown's formula $\mathbf{F}_{\text{const}}^{\text{Br}}$ in (2.2) and the continuum limit formula $\mathbf{F}_{\text{const}}^{\text{lim}}$ in (2.4) are considered. For notational simplicity, we will in the following denote these formulae by \mathbf{F}^{Br} and \mathbf{F}^{lim} , respectively.

All numerical experiments are performed in MATLAB, where the computations are done in IEEE double precision arithmetics. The numerical outcome is visualized as follows: In each experiment, we first plot the force $\mathbf{F}(\varepsilon, L)$ in dependence on the positive distance $\varepsilon > 0$ for a fixed value of the geometry parameter $L > 0$. We vary ε in the interval $(0, 5]$, with stepsize 10^{-9} , and graph the corresponding curves for L in the discrete set $\{1, \dots, 20\}$. The results are illustrated both in the full range of $\varepsilon \in (0, 5]$ and in a zoom on the ε -interval $(0, 0.1]$.

Secondly, for $\varepsilon = 0$, we plot Brown's force formula $\mathbf{F}^{\text{Br}}(L)$ and the continuum limit force $\mathbf{F}^{\text{lim}}(L)$ in dependence on $L \in (0, 20]$, where the stepsize is again 10^{-9} . Moreover, in an accompanying table we provide the numerical values of \mathbf{F}^{Br} and \mathbf{F}^{lim} for the discrete set of L -values $\{\frac{1}{16}, \frac{1}{8}, \frac{1}{4}, \frac{1}{2}, 1, 2, 4, 8, 16\}$, as well as the deviation with respect to \mathbf{F}^{lim} .






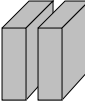
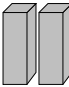

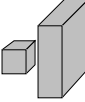
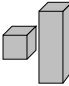
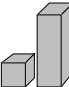

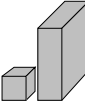
2D Experiments		3D Experiments	
Experiment	Configuration	Experiment	Configuration
1 _{2D}		1 _{3D}	
2 _{2D} *		2 _{3D} *	
3 _{2D}		3 _{3D}	
		4 _{3D}	
4 _{2D}		5 _{3D}	
		6 _{3D} *	
		7 _{3D} *	
5 _{2D} *		8 _{3D} *	

TABLE 3.1. Overview of the numerical experiments presented in Section 3. The rows of the table show analogous experiments in two and three dimensions. The specific setup of each experiment is given in detail in the corresponding subsection. The asterisks indicate experiments which are not illustrated graphically below for brevity.

3.1. The Two-Dimensional Case. Let A and B be two magnetic bodies specified in detail in the experiments below. We denote by B_ε the translation of B in 1-direction, i.e., $B_\varepsilon := \{x + (\varepsilon, 0) \mid x \in B\}$. By definition, there holds $B_0 = B$. For the magnetizations, we take $\mathbf{m}_A = (1, 0)$ and $\mathbf{m}_{B_\varepsilon} = (1, 0)$ throughout, which implies that A and B attract each other.

In all five experiments, we first compute $\mathbf{F}(\varepsilon, L) = \mathbf{F}(A, B_\varepsilon)$ in dependence on the distance parameter $\varepsilon > 0$ and the length or height parameter $L > 0$. Since the second component $\mathbf{F}_2(\varepsilon, L)$ of $\mathbf{F}(\varepsilon, L)$ is identically zero in most of the experiments and since it is qualitatively similar to the first component $\mathbf{F}_1(\varepsilon, L)$ in the others, the presentation is restricted to \mathbf{F}_1 throughout. For $\varepsilon = 0$, we additionally evaluate \mathbf{F}^{Br} and \mathbf{F}^{lim} , see (2.2) and (2.4), and we study the difference between \mathbf{F}^{Br} and \mathbf{F}^{lim} in dependence on $L > 0$.

3.1.1. Experiment 1_{2D}. Given $L > 0$, we define

$A = \text{conv}\{(0, 0), (1, 0), (1, 1), (0, 1)\}$ and $B = \text{conv}\{(1, 0), (1 + L, 0), (1 + L, 1), (1, 1)\}$,
i.e., A is the unit square and B is a rectangle of length L and height 1.

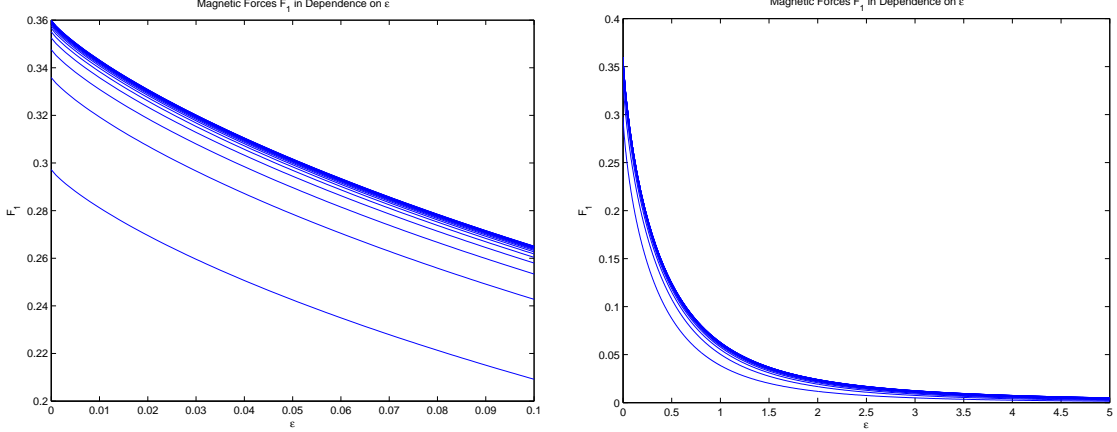


FIGURE 3.1. The force $\mathbf{F}_1(\varepsilon, L)$ in Experiment 1_{2D} in dependence on $\varepsilon \in (0, 0.1]$ (left panel) and $\varepsilon \in (0, 5]$ (right panel). Both panels show curves for varying length $L = 1, \dots, 20$, where $L = 1$ (respectively $L = 20$) corresponds to the downmost curve (respectively to the uppermost curve). As expected, we observe (monotone) convergence as $L \rightarrow \infty$, cf. (3.3), with $\lim_{\varepsilon \rightarrow 0} \lim_{L \rightarrow \infty} \mathbf{F}_1(\varepsilon, L) \approx 0.360$.

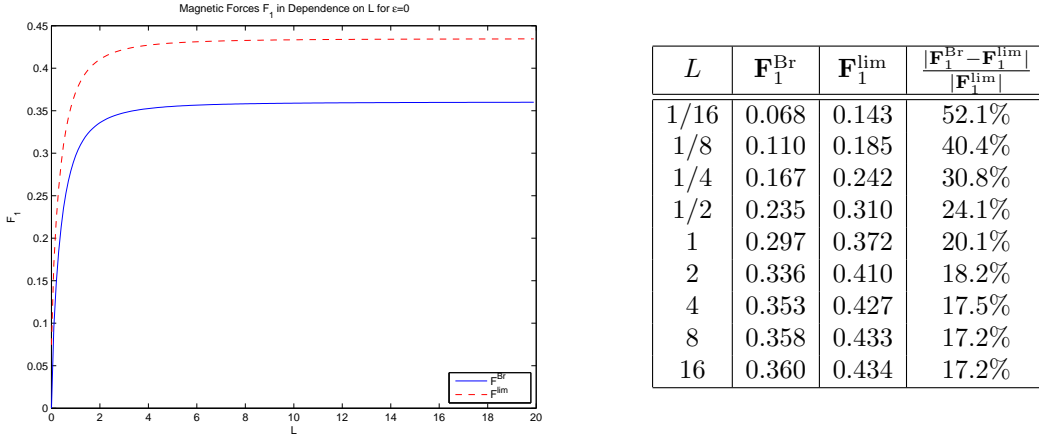


FIGURE 3.2. The forces \mathbf{F}_1^{Br} (solid) and $\mathbf{F}_1^{\text{lim}}$ (dashed) in Experiment 1_{2D} in dependence on L for $\varepsilon = 0$. Analytically, in the limits of $L \rightarrow 0^+$ and $L \rightarrow \infty$, one expects $\mathbf{F}_1^{\text{Br}}(0^+) = 0$ and $\mathbf{F}_1^{\text{lim}}(0^+) \approx 0.075$ respectively $\mathbf{F}_1^{\text{Br}}(\infty) \approx 0.360$ and $\mathbf{F}_1^{\text{lim}}(\infty) \approx 0.435$, which is also observed numerically. In addition to the graphical illustration (left panel), the table in the right panel gives the numerical values of the forces for certain L -values as well as the deviation with respect to $\mathbf{F}_1^{\text{lim}}$.

Recall that for $\varepsilon, L > 0$, $\mathbf{F}_1(\varepsilon, L)$ denotes the first component of \mathbf{F} in dependence on ε and L . The plot in Figure 3.1 shows that $\mathbf{F}_1(\varepsilon, L)$ increases with decreasing distance ε and that it converges to a finite value as $\varepsilon \rightarrow 0$. Moreover, for increasing L , the corresponding curves converge in a

monotonically increasing fashion to a limit curve. Both these observations can also be understood analytically: In Experiment 1_{2D}, the force $\mathbf{F}(\varepsilon, L)$ reads

$$(3.1) \quad \begin{aligned} & \mathbf{F}(\varepsilon, L) \\ &= - \int_{[(0,0),(0,1)]} \left(\int_{[(1+\varepsilon,0),(1+\varepsilon,1)]} \nabla N(x-y) ds_y - \int_{[(1+L+\varepsilon,0),(1+L+\varepsilon,1)]} \nabla N(x-y) ds_y \right) ds_x \\ & \quad - \int_{[(1,0),(1,1)]} (-1) \left(\int_{[(1+\varepsilon,0),(1+\varepsilon,1)]} \nabla N(x-y) ds_y - \int_{[(1+L+\varepsilon,0),(1+L+\varepsilon,1)]} \nabla N(x-y) ds_y \right) ds_x, \end{aligned}$$

cf. (2.1). In particular, there holds

$$\mathbf{F}_1(\varepsilon, L) = -I(1+\varepsilon) + I(1+L+\varepsilon) + I(\varepsilon) - I(L+\varepsilon),$$

cf. Lemma B.1, where the function $I(s)$ is defined by

$$(3.2) \quad I(s) = \frac{1}{2\pi} \left(2 \arctan \frac{1}{s} - s \ln \left(1 + \frac{1}{s^2} \right) \right) \quad \text{for all } s \in \mathbb{R} \setminus \{0\}.$$

For $s > 0$, $I(s)$ is positive, strictly monotonically decreasing, and strictly convex, since $I'(s) = -\frac{1}{2\pi} \ln(1 + \frac{1}{s^2}) < 0$ is strictly monotonically increasing. Hence,

$$(3.3) \quad \mathbf{F}_1(\varepsilon, L) - \mathbf{F}_1(\varepsilon, \ell) = I(1+L+\varepsilon) - I(L+\varepsilon) - (I(1+\ell+\varepsilon) - I(\ell+\varepsilon)) > 0$$

for $L > \ell$, i.e., $\mathbf{F}_1(\varepsilon, L)$ is strictly monotonically increasing with L . Since $I(s)$ tends to zero as $s \rightarrow \infty$, we conclude that $\mathbf{F}_1(\varepsilon, L)$ converges as $L \rightarrow \infty$. Indeed, there holds

$$\begin{aligned} \lim_{L \rightarrow \infty} \mathbf{F}_1(\varepsilon, L) &= -I(1+\varepsilon) + I(\varepsilon) \\ &= \frac{1}{2\pi} \left(-2 \arctan \frac{1}{1+\varepsilon} + (1+\varepsilon) \ln \left(1 + \frac{1}{(1+\varepsilon)^2} \right) + 2 \arctan \frac{1}{\varepsilon} - \varepsilon \ln \left(1 + \frac{1}{\varepsilon^2} \right) \right). \end{aligned}$$

Furthermore, we obtain

$$(3.4) \quad \lim_{\varepsilon \rightarrow 0} \mathbf{F}_1(\varepsilon, L) = -I(1) + I(1+L) + I(0) - I(L) \quad \text{for all } L > 0,$$

where $I(0) = \lim_{s \rightarrow 0} I(s) = \frac{1}{2}$. For $L \rightarrow \infty$, we thus have

$$\lim_{\varepsilon \rightarrow 0} \lim_{L \rightarrow \infty} \mathbf{F}_1(\varepsilon, L) = -I(1) + I(0) = \frac{1}{2\pi} (-2 \arctan 1 + \ln 2) + \frac{1}{2} = \frac{1}{4} + \frac{\ln 2}{2\pi} \approx 0.360,$$

which agrees with the numerical results shown in Figure 3.1.

We now turn to $\varepsilon = 0$: First, note that the second term in Brown's formula (2.2) is easily obtained as

$$(3.5) \quad \frac{1}{2} \int_{\partial A \cap \partial B} (\mathbf{m}_A \cdot \mathbf{n}_A)(\mathbf{m}_B \cdot \mathbf{n}_A) \mathbf{n}_A ds_x = \frac{1}{2} |\partial A \cap \partial B| (1, 0).$$

The short-range part of the continuum limit formula (2.4) involves the tensor $(S_{ijkp})_{i,j,k,p=1,2}$, cf. [PPS, Equation (3.22)], which depends on the underlying lattice structure. For simplicity, we assume that the lattice \mathcal{L} is the square lattice, $\mathcal{L} = \mathbb{Z}^2$. As shown in [PPS, Appendix A], all entries of $(S_{ijkp})_{i,j,k,p=1,2}$ are then zero by symmetry, except for the four terms $S_{iikk} = S_{ikki} = S_{kiki} = -\mathcal{S} + \frac{1}{4}$ with $i \neq k$ and $S_{kkkk} = \mathcal{S} + \frac{3}{4}$, where $\mathcal{S} \approx \frac{1}{2\pi} 2.50765$ is a constant that can be computed numerically,

cf. [PPS, Appendix A]. For k fixed, we thus have

$$\begin{aligned} \sum_{i,j,p=1}^2 S_{ijkp}(\mathbf{m}_A)_i(\mathbf{m}_B)_j(\mathbf{n}_A)_p &= S_{kkkk}(\mathbf{m}_A)_k(\mathbf{m}_B)_k(\mathbf{n}_A)_k \\ &+ S_{ikk} \sum_{\substack{i=1 \\ i \neq k}}^2 ((\mathbf{m}_A)_i(\mathbf{m}_B)_i(\mathbf{n}_A)_k + (\mathbf{m}_A)_k(\mathbf{m}_B)_i(\mathbf{n}_A)_i + (\mathbf{m}_A)_i(\mathbf{m}_B)_k(\mathbf{n}_A)_i). \end{aligned}$$

With $(\mathbf{m}_A)_i = \delta_{1i} = (\mathbf{m}_B)_i$ and $(\mathbf{n}_A)_i = \delta_{1i}$ on $\partial A \cap \partial B$, this expression reduces to

$$\sum_{i,j,p=1}^2 S_{ijkp}(\mathbf{m}_A)_i(\mathbf{m}_B)_j(\mathbf{n}_A)_p = S_{1111}\delta_{1k}.$$


Hence, we obtain

$$(3.6) \quad \mathbf{F}^{\text{short}} = \frac{1}{2} \sum_{i,j,p=1}^2 (S_{ij1p}, S_{ij2p}) \int_{\partial A \cap \partial B} (\mathbf{m}_A)_i(\mathbf{m}_B)_j(\mathbf{n}_A)_p ds_x = \frac{1}{2}(S_{1111}, 0)|\partial A \cap \partial B|.$$

In Figure 3.2, we plot \mathbf{F}_1^{Br} and $\mathbf{F}_1^{\text{lim}}$ for $\varepsilon = 0$ fixed in dependence on $L \in (0, 20]$, where $L \approx 0$ corresponds to a thin film B . While \mathbf{F}_1^{Br} tends to zero as $L \rightarrow 0$, the limiting force converges to a positive value. The right panel in Figure 3.2 gives explicit values of the forces for $L = \frac{1}{16}, \frac{1}{8}, \dots, 8, 16$, as well as the deviation with respect to $\mathbf{F}_1^{\text{lim}}$. As is shown in [PPS, Section 2], there holds $\mathbf{F}_1^{\text{Br}}(L) = \lim_{\varepsilon \rightarrow 0} \mathbf{F}_1(\varepsilon, L)$. Analytically, we observe that for fixed $L > 0$, (3.4) becomes

$$\begin{aligned} \lim_{\varepsilon \rightarrow 0} \mathbf{F}_1(\varepsilon, L) &= \frac{1}{2\pi} \left(\frac{\pi}{2} + \ln 2 + 2 \arctan \frac{1}{1+L} - (1+L) \ln \left(1 + \frac{1}{(1+L)^2} \right) - 2 \arctan \frac{1}{L} \right. \\ &\quad \left. + L \ln \left(1 + \frac{1}{L^2} \right) \right) \\ &= \mathbf{F}_1^{\text{Br}}(L). \end{aligned}$$

By (2.3) and (2.4) in combination with (3.5) and (3.6), $\mathbf{F}_1^{\text{lim}}(L) = \mathbf{F}_1^{\text{Br}}(L) + \frac{1}{2}(S_{1111} - 1)$ for all $L > 0$, i.e., the difference between $\mathbf{F}_1^{\text{lim}}(L)$ and $\mathbf{F}_1^{\text{Br}}(L)$ is independent of L . Since $\mathbf{F}_1^{\text{Br}}(0^+) := \lim_{L \rightarrow 0} \mathbf{F}_1^{\text{Br}}(L) = 0$, this implies $\mathbf{F}_1^{\text{lim}}(0^+) := \lim_{L \rightarrow 0} \mathbf{F}_1^{\text{lim}}(L) = \frac{1}{2}(S_{1111} - 1) \approx 0.075$ for $\mathcal{L} = \mathbb{Z}^2$, which can also be observed in Figure 3.2. On the other hand, we know that for large L , $\mathbf{F}_1^{\text{Br}}(\infty) := \lim_{L \rightarrow \infty} \mathbf{F}_1^{\text{Br}}(L) = \frac{1}{4} + \frac{\ln 2}{2\pi} \approx 0.360$. Hence, $\mathbf{F}_1^{\text{lim}}(\infty) := \lim_{L \rightarrow \infty} \mathbf{F}_1^{\text{lim}}(L) = \frac{\ln 2}{2\pi} + \frac{1}{2}S_{1111} - \frac{1}{4} \approx 0.435$, see again Figure 3.2.

3.1.2. Experiment 2_{2D}.  In the second experiment, we vary the length L of both A and B simultaneously, with

$$A = \text{conv}\{(0, 0), (L, 0), (L, 1), (0, 1)\} \quad \text{and} \quad B = \text{conv}\{(L, 0), (2L, 0), (2L, 1), (L, 1)\},$$

i.e., A and B are rectangular and of equal size. The numerical results are similar to the ones obtained in Experiment 1_{2D} above and are therefore not illustrated here for brevity. Correspondingly, analytical formulae for \mathbf{F} , \mathbf{F}^{Br} , and \mathbf{F}^{lim} can be derived analogously as in Experiment 1_{2D}.

In particular, $\mathbf{F}_1(\varepsilon, L) = -2I(L + \varepsilon) + I(2L + \varepsilon) + I(\varepsilon)$, with $I(s)$ from (3.2). The monotonicity argument for the force in dependence on L is also similar to the one given above. The limiting

value of $\mathbf{F}_1(\varepsilon, L)$ for $L \rightarrow \infty$ and $\varepsilon \rightarrow 0$ is $I(0) = \frac{1}{2}$ now. Furthermore, we have

$$\begin{aligned} \lim_{\varepsilon \rightarrow 0} \mathbf{F}_1(\varepsilon, L) &= -2I(L) + I(2L) + \frac{1}{2} \\ &= \frac{1}{2\pi} \left(-4 \arctan \frac{1}{L} + 2L \ln \left(1 + \frac{1}{L^2} \right) + 2 \arctan \frac{1}{2L} - 2L \ln \left(1 + \frac{1}{(2L)^2} \right) \right) + \frac{1}{2} \\ &= \mathbf{F}_1^{\text{Br}}(L) = \mathbf{F}_1^{\text{lim}}(L) - \frac{1}{2}(S_{1111} - 1); \end{aligned}$$

note that the difference $\mathbf{F}_1^{\text{Br}} - \mathbf{F}_1^{\text{lim}}$ is independent of L . In the limit of $L \rightarrow 0^+$, we obtain $\mathbf{F}_1^{\text{Br}}(0^+) = 0$ and $\mathbf{F}_1^{\text{lim}}(0^+) = \frac{1}{2}(S_{1111} - 1) \approx 0.075$. For $L \rightarrow \infty$, \mathbf{F}_1^{Br} and $\mathbf{F}_1^{\text{lim}}$ converge to $\mathbf{F}_1^{\text{Br}}(\infty) = \frac{1}{2}$ and to $\mathbf{F}_1^{\text{lim}}(\infty) = \frac{1}{2}S_{1111} \approx 0.575$, respectively. However, this analytical limit $\lim_{\varepsilon \rightarrow 0} \lim_{L \rightarrow \infty} \mathbf{F}_1(\varepsilon, L) = \frac{1}{2}$ is observed numerically only if $L \gg 20$: For $L = 1000$, one finds e.g. $\lim_{\varepsilon \rightarrow 0} F_1(\varepsilon, 1000) \approx 0.4998$, which is in good agreement with the numerical outcome (not shown).

3.1.3. Experiment 3_{2D}.



In the third experiment, we consider two rectangles of varying height L ,

$$A = \text{conv}\{(0, 0), (1, 0), (1, L), (0, L)\} \quad \text{and} \quad B = \text{conv}\{(1, 0), (2, 0), (2, L), (1, L)\}.$$

The plots in Figure 3.3 indicate that $\mathbf{F}_1(\varepsilon, L)$ converges uniformly to a limit curve as $L \rightarrow \infty$. All curves increase with decreasing ε and converge to finite values as $\varepsilon \rightarrow 0$. However, while \mathbf{F}_1^{Br} is convergent as $L \rightarrow \infty$, Figure 3.4 shows that $\mathbf{F}_1^{\text{lim}}$ diverges. Hence, the difference between $\mathbf{F}_1^{\text{lim}}$ and \mathbf{F}_1^{Br} , and therefore also the relative deviation between the two, increases with L . For $L \rightarrow 0$, the volume of the two bodies converges to zero; according to the plots, both forces tend to zero in this limit.

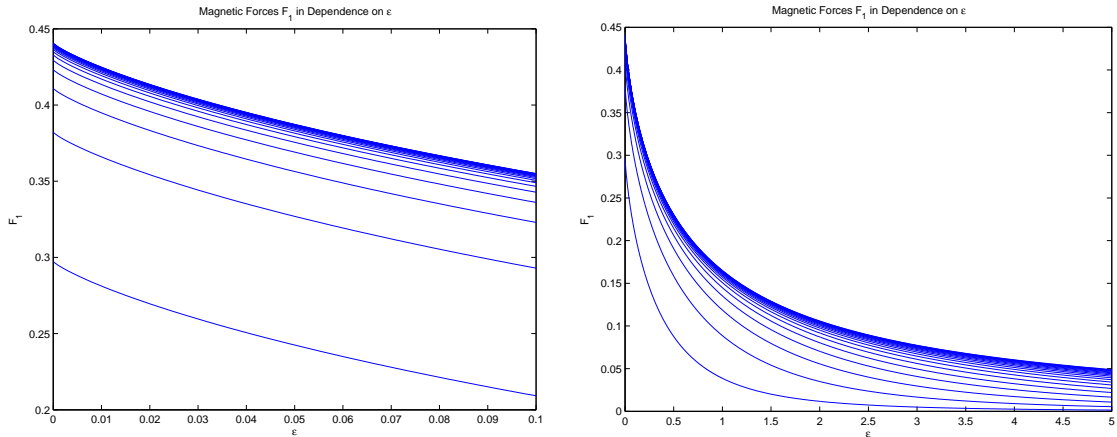
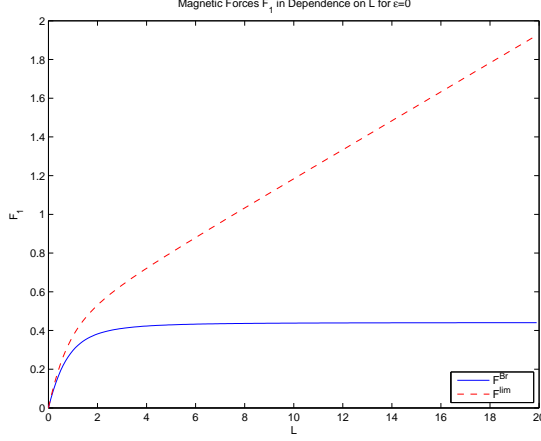


FIGURE 3.3. The force $\mathbf{F}_1(\varepsilon, L)$ in Experiment 3_{2D} in dependence on $\varepsilon \in (0, 0.1]$ (left panel) and $\varepsilon \in (0, 5]$ (right panel). Both figures show curves for varying height $L = 1, \dots, 20$, where $L = 1$ (respectively $L = 20$) corresponds to the downmost curve (respectively to the uppermost curve). As expected, we observe (monotone) convergence as $L \rightarrow \infty$, with $\lim_{\varepsilon \rightarrow 0} \lim_{L \rightarrow \infty} \mathbf{F}_1(\varepsilon, L) = 0.441$.



L	\mathbf{F}_1^{Br}	$\mathbf{F}_1^{\text{lim}}$	$\frac{ \mathbf{F}_1^{\text{Br}} - \mathbf{F}_1^{\text{lim}} }{ \mathbf{F}_1^{\text{lim}} }$
1/16	0.030	0.035	13.3%
1/8	0.059	0.068	13.7%
1/4	0.110	0.129	14.5%
1/2	0.193	0.230	16.2%
1	0.297	0.372	20.1%
2	0.382	0.531	28.1%
4	0.423	0.721	41.3%
8	0.436	1.033	57.7%
16	0.440	1.633	73.1%

FIGURE 3.4. The forces \mathbf{F}_1^{Br} (solid) and $\mathbf{F}_1^{\text{lim}}$ (dashed) in Experiment 3_{2D} in dependence on L for $\varepsilon = 0$. Note that our analysis predicts $\mathbf{F}_1^{\text{Br}}(0^+) = 0 = \mathbf{F}_1^{\text{lim}}(0^+)$ as well as $\mathbf{F}_1^{\text{Br}}(\infty) = 0.441$ and $\mathbf{F}_1^{\text{lim}}(L) \approx \mathbf{F}_1^{\text{Br}}(L) + 0.075 \cdot L$. Hence, we expect linear growth of $\mathbf{F}_1^{\text{lim}}(L)$ with slope 0.075 as $L \rightarrow \infty$, which is indeed observed numerically. In addition to the graphical illustration (left panel), the table in the right panel gives the numerical values of the forces for certain L -values as well as the deviation with respect to $\mathbf{F}_1^{\text{lim}}$.

Let $I(s, L) = \frac{1}{2\pi}(2L \arctan \frac{L}{s} - s \ln(1 + \frac{L^2}{s^2}))$. Then, by Lemma B.1, the first component of the force is given by

$$\begin{aligned} \mathbf{F}_1(\varepsilon, L) &= -2I(1 + \varepsilon, L) + I(2 + \varepsilon, L) + I(\varepsilon, L) \\ &= \frac{1}{2\pi} \left(-4L \arctan \frac{L}{1 + \varepsilon} + 2(1 + \varepsilon) \ln \left(1 + \frac{L^2}{(1 + \varepsilon)^2} \right) + 2L \arctan \frac{L}{2 + \varepsilon} \right. \\ &\quad \left. - (2 + \varepsilon) \ln \left(1 + \frac{L^2}{(2 + \varepsilon)^2} \right) + 2L \arctan \frac{L}{\varepsilon} - \varepsilon \ln \left(1 + \frac{L^2}{\varepsilon^2} \right) \right) \end{aligned}$$

for $\varepsilon, L > 0$. Again, we observe monotonicity with increasing L . Indeed, $\frac{\partial}{\partial L} I(s, L) = \frac{1}{\pi} \arctan \frac{L}{s} > 0$ for all $s > 0$, and $\frac{\partial}{\partial s} I(s, L) = -\frac{1}{2} \ln(1 + \frac{L^2}{s^2}) < 0$ is strictly monotonically increasing. Hence, if $L > \ell$, $\mathbf{F}_1(\varepsilon, L) - \mathbf{F}_1(\varepsilon, \ell) > 0$ for every $\varepsilon > 0$. In the limit of $L \rightarrow \infty$, we obtain

$$\lim_{L \rightarrow \infty} \mathbf{F}_1(\varepsilon, L) = \frac{1}{2\pi} \left(4 \ln \frac{2 + \varepsilon}{1 + \varepsilon} + \varepsilon \ln \frac{\varepsilon^2(2 + \varepsilon)^2}{(1 + \varepsilon)^4} \right) \xrightarrow{\varepsilon \rightarrow 0} \frac{2 \ln 2}{\pi} \approx 0.441.$$

Brown's formula equals the limit of $\mathbf{F}_1(\varepsilon, L)$ as $\varepsilon \rightarrow 0$ and reads

$$\begin{aligned} \mathbf{F}_1^{\text{Br}}(L) &= \frac{1}{2\pi} \left(-4L \arctan L + 2 \ln \frac{4(1 + L^2)}{4 + L^2} + 2L \arctan \frac{L}{2} - 2 \ln \left(1 + \frac{L^2}{4} \right) + L\pi \right) \\ &= \mathbf{F}_1^{\text{lim}}(L) - \frac{1}{2}L(S_{1111} - 1). \end{aligned}$$

Therefore, the difference between $\mathbf{F}_1^{\text{lim}}(L)$ and $\mathbf{F}_1^{\text{Br}}(L)$ grows linearly with the height L , and there holds $\mathbf{F}_1^{\text{Br}}(\infty) = \lim_{L \rightarrow \infty} \mathbf{F}_1^{\text{Br}}(L) = \frac{2 \ln 2}{\pi} \approx 0.441$. Note that both forces converge to zero as $L \rightarrow 0^+$, i.e., we have $\mathbf{F}_1^{\text{Br}}(0^+) = 0 = \mathbf{F}_1^{\text{lim}}(0^+)$, which is also observed in Figure 3.4.

3.1.4. Experiment 4_{2D}.



For a given height $L > 0$, we define

$$A = \text{conv}\left\{\left(0, -\frac{1}{2}\right), \left(1, -\frac{1}{2}\right), \left(1, \frac{1}{2}\right), \left(0, \frac{1}{2}\right)\right\} \quad \text{and}$$

$$B = \text{conv}\left\{\left(1, -\frac{L}{2}\right), \left(2, -\frac{L}{2}\right), \left(2, \frac{L}{2}\right), \left(1, \frac{L}{2}\right)\right\}.$$

According to the numerical results presented in Figure 3.5, the force $\mathbf{F}_1(\varepsilon, L)$ converges to zero pointwise with increasing L . However, in contrast to the preceding three experiments, the corresponding curves are not monotone in L for $\varepsilon > 0$ fixed. Figure 3.6 shows that \mathbf{F}_1^{Br} and $\mathbf{F}_1^{\text{lim}}$ both attain their maximum values at $L = 1$ and that they are both zero for $L = 0$. Moreover, \mathbf{F}_1^{Br} converges to zero as $L \rightarrow \infty$, whereas $\mathbf{F}_1^{\text{lim}}$ approaches a positive value.

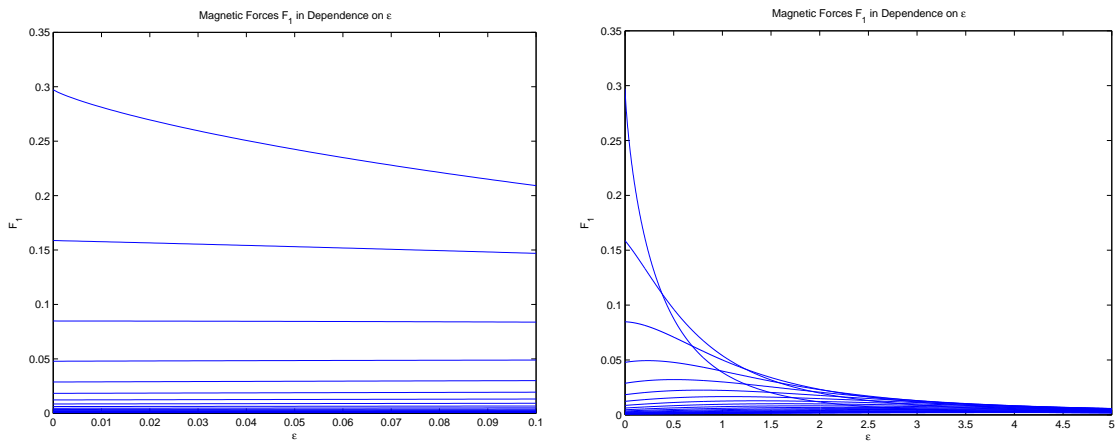


FIGURE 3.5. The force $\mathbf{F}_1(\varepsilon, L)$ in Experiment 4_{2D} in dependence on $\varepsilon \in (0, 0.1]$ (left panel) and $\varepsilon \in (0, 5]$ (right panel). Both panels show curves for varying height $L = 1, \dots, 20$, where $L = 1$ (respectively $L = 20$) corresponds to the uppermost curve (respectively to the downmost curve) for ε small (left panel). The force tends to zero pointwise as $L \rightarrow \infty$. Note, however, that the convergence is not monotone in L for ε fixed (right panel).

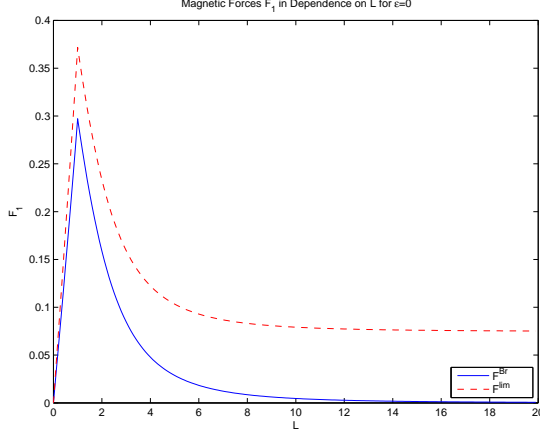
Again, these empirical observations can be understood analytically. To that end, one can proceed as in Experiment 1_{2D} to verify $\mathbf{F}_1(\varepsilon, L) = -2I(1 + \varepsilon, L) + I(2 + \varepsilon, L) + I(\varepsilon, L)$, where $I(s, L)$ is given by

$$I(s, L) = \frac{1}{2\pi} \left((1 - L) \arctan \frac{L - 1}{2s} + s \ln \frac{s^2 + (L - 1)^2}{s^2 + (L + 1)^2} + (1 + L) \arctan \frac{L + 1}{2s} \right)$$

according to Lemma B.1. The force converges pointwise to zero as $L \rightarrow \infty$. However, as indicated above, the curves are not monotone in L now. (Analytically, this can be seen by evaluating \mathbf{F}_1 for fixed ε and appropriately chosen L -values.)

In the limit as $s \rightarrow 0$, we have

$$I(0, L) = \begin{cases} \frac{1}{2\pi} \left((1 - L) \frac{\pi}{2} + (1 + L) \frac{\pi}{2} \right) = \frac{1}{2} & \text{if } L \geq 1, \\ \frac{1}{2\pi} \left(-(1 - L) \frac{\pi}{2} + (1 + L) \frac{\pi}{2} \right) = \frac{L}{2} & \text{if } L < 1. \end{cases}$$



L	\mathbf{F}_1^{Br}	$\mathbf{F}_1^{\text{lim}}$	$\frac{ \mathbf{F}_1^{\text{Br}} - \mathbf{F}_1^{\text{lim}} }{ \mathbf{F}_1^{\text{lim}} }$
1/16	0.018	0.022	20.9%
1/8	0.035	0.045	20.8%
1/4	0.071	0.090	20.8%
1/2	0.143	0.181	20.6%
1	0.297	0.372	20.1%
2	0.159	0.233	32.0%
4	0.048	0.122	60.9%
8	0.009	0.083	89.7%
16	0.001	0.076	98.4%

FIGURE 3.6. The forces \mathbf{F}_1^{Br} (solid) and $\mathbf{F}_1^{\text{lim}}$ (dashed) in Experiment $4_{2\text{D}}$ in dependence on L for $\varepsilon = 0$. Note that both curves have an absolute maximum at $L = 1$. The numerical results provide empirical support for the analysis, which predicts $\mathbf{F}_1^{\text{Br}}(\infty) = 0$ and $\mathbf{F}_1^{\text{lim}}(\infty) \approx 0.075$ as well as $\mathbf{F}_1^{\text{Br}}(0^+) = 0 = \mathbf{F}_1^{\text{lim}}(0^+)$. In addition to the graphical illustration (left panel), the table in the right panel gives the numerical values of the forces for certain L -values as well as the deviation with respect to $\mathbf{F}_1^{\text{lim}}$.

This yields the following analytical expressions for the curves plotted in Figure 3.6:

$$\begin{aligned}
\mathbf{F}_1^{\text{Br}}(L) &= \lim_{\varepsilon \rightarrow 0} \mathbf{F}_1(\varepsilon, L) \\
&= \frac{1}{2\pi} \left(2(1-L) \arctan \frac{L-1}{2} - 2 \ln \frac{1+(L-1)^2}{1+(L+1)^2} \right. \\
&\quad - 2(1+L) \arctan \frac{L+1}{2} + (1-L) \arctan \frac{L-1}{4} + 2 \ln \frac{4+(L-1)^2}{4+(L+1)^2} \\
&\quad \left. + (1+L) \arctan \frac{L+1}{4} + (1+L-|1-L|) \frac{\pi}{2} \right), \\
\mathbf{F}_1^{\text{lim}}(L) &= \mathbf{F}_1^{\text{Br}}(L) + \frac{1}{2} \min\{1, L\} (S_{1111} - 1).
\end{aligned}$$

Interestingly, $\mathbf{F}_1^{\text{Br}}(L)$ tends to zero as $L \rightarrow \infty$, i.e., Brown's formula predicts that $\mathbf{F}_1^{\text{Br}}(\infty) = 0$ in this setting. Physically speaking, this implies the following: If, for L sufficiently large, the whole setting were rotated by $\frac{\pi}{2}$ and placed in a gravitational field (even a weak one), the magnet A would “fall off,” since there would be almost no magnetic force present according to Brown's formula. The limiting force $\mathbf{F}_1^{\text{lim}}$, however, does give an attracting contribution, with $\mathbf{F}_1^{\text{lim}}(\infty) = \frac{1}{2}(S_{1111} - 1) \approx 0.075$ as $L \rightarrow \infty$, cf. also Experiment $5_{2\text{D}}$ below.

3.1.5. Experiment $5_{2\text{D}}$.  Finally, for $L > 0$ we set

$$A = \text{conv}\{(0, 0), (1, 0), (1, 1), (0, 1)\} \quad \text{and} \quad B = \text{conv}\{(1, 0), (2, 0), (2, L), (1, L)\}.$$

As in $4_{2\text{D}}$, we observe pointwise convergence of $\mathbf{F}_1(\varepsilon, L)$ with increasing L ; however, contrary to Experiment $4_{2\text{D}}$, the limit $\lim_{L \rightarrow \infty} \mathbf{F}_1(\varepsilon, L)$ is not zero. In particular, it turns out that the force is attracting at $\varepsilon = 0$ for all $L > 0$. Accordingly, Brown's force \mathbf{F}_1^{Br} approaches a positive value as

$L \rightarrow \infty$. Otherwise, the numerical results (not shown) are qualitatively similar to the ones given in Figure 3.6 above.

Analytically, we obtain $\mathbf{F}_1(\varepsilon, L) = -2I(1 + \varepsilon, L) + I(2 + \varepsilon, L) + I(\varepsilon, L)$ now, with

$$I(s, L) = \frac{1}{2\pi} \left((1-L) \arctan \frac{L-1}{s} + \frac{s}{2} \ln \frac{s^2 + (L-1)^2}{s^2 + (L^2+1) + \frac{L^2}{s^2}} + \arctan \frac{1}{s} + L \arctan \frac{L}{s} \right).$$

Again, we have no monotonicity of the force with L . The limit of the force as $L \rightarrow \infty$ is given by

$$\begin{aligned} \lim_{L \rightarrow \infty} \mathbf{F}_1(\varepsilon, L) &= \frac{1}{2\pi} \left((1+\varepsilon) \ln \left(1 + \frac{1}{(1+\varepsilon)^2} \right) - 2 \arctan \frac{1}{1+\varepsilon} - \frac{2+\varepsilon}{2} \ln \left(1 + \frac{1}{(2+\varepsilon)^2} \right) \right. \\ &\quad \left. + \arctan \frac{1}{2+\varepsilon} - \frac{\varepsilon}{2} \ln \left(1 + \frac{1}{\varepsilon^2} \right) + \arctan \frac{1}{\varepsilon} \right) \\ &\xrightarrow{\varepsilon \rightarrow 0} \frac{1}{2\pi} \left(\arctan \frac{1}{2} + \ln \frac{8}{5} \right) \approx 0.1486. \end{aligned}$$

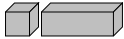
Moreover, Brown's formula becomes

$$\begin{aligned} \mathbf{F}_1^{\text{Br}}(L) &= -2I(1, L) + I(2, L) + I(0, L) \\ &= \frac{1}{2\pi} \left(-2(1-L) \arctan(L-1) - \ln \left(1 + \frac{(L-1)^2}{2+2L^2} \right) - \frac{\pi}{2} - 2L \arctan L \right. \\ &\quad \left. + (1-L) \arctan \frac{L-1}{2} + \ln \left(4 + \frac{(L-1)^2}{5 + \frac{5}{4}L^2} \right) + \arctan \frac{1}{2} + L \arctan \frac{L}{2} + \frac{L+1-|L-1|}{4} \right) \\ &= \mathbf{F}_1^{\text{lim}}(L) - \frac{1}{2} \min\{1, L\} (S_{1111} - 1). \end{aligned}$$

As $L \rightarrow 0$, both \mathbf{F}_1^{Br} and $\mathbf{F}_1^{\text{lim}}$ converge to zero. Finally, in the limit of $L \rightarrow \infty$, we obtain $\mathbf{F}_1^{\text{Br}}(\infty) = \frac{1}{2\pi} (\arctan \frac{1}{2} + \ln \frac{8}{5}) \approx 0.149$ and $\mathbf{F}_1^{\text{lim}}(\infty) = \frac{1}{2\pi} (\arctan \frac{1}{2} + \ln \frac{8}{5}) + \frac{1}{2} (S_{1111} - 1) \approx 0.224$, respectively.

3.2. The Three-Dimensional Case. In three dimensions, we assume the two magnetic bodies A and B to be cuboidal, where A is fixed in space and B is moving towards it. Moreover, we only consider constant magnetizations, with $\mathbf{m}_A = (1, 0, 0)$ and $\mathbf{m}_B = (1, 0, 0)$ throughout. In analogy to the two-dimensional case, we define $B_\varepsilon := \{x + (\varepsilon, 0, 0) \mid x \in B\}$ by default. Also, we again vary the length, height, and depth of A and B , respectively. In all experiments, we compute $\mathbf{F}(\varepsilon, L) = \mathbf{F}(A, B_\varepsilon)$ in dependence on the distance parameter $\varepsilon > 0$ and a geometry parameter $L > 0$ which is specified below. Since the second and the third component of $\mathbf{F}(\varepsilon, L)$ are identically zero in most of the experiments, the presentation is again restricted to $\mathbf{F}_1(\varepsilon, L)$ in the following. For $\varepsilon = 0$, we additionally compute $\mathbf{F}_1^{\text{Br}}(L)$ and $\mathbf{F}_1^{\text{lim}}(L)$ in dependence on $L > 0$, and we study the difference between the two formulae.

As in the two-dimensional case, one can, in principle, again derive analytical expressions for the above force formulae and study their limits as well as their monotonicity behavior, cf. [Pab06]. The derivation involves formulae as quoted in Section 2.2 and Appendix A.2. However, since the resulting expressions are lengthy and somewhat analogous to the ones obtained for $d = 2$, we focus exclusively on the interpretation of our numerical results below and refer to [Pab06] for the analytical details.

3.2.1. Experiment 1_{3D}.  Let A be the unit cube, and let B be a cuboid of length $L > 0$ and height and depth 1, i.e., we consider the analog of Experiment 1_{2D} in a three-dimensional

setting, with

$$A = \text{conv}\{(0, 0, 0), (0, 1, 0), (0, 1, 1), (0, 0, 1), (1, 0, 0), (1, 1, 0), (1, 1, 1), (1, 0, 1)\} \quad \text{and}$$

$$B = \text{conv}\{(1, 0, 0), (1, 1, 0), (1, 1, 1), (1, 0, 1), (1 + L, 0, 0), (1 + L, 1, 0), (1 + L, 1, 1), (1 + L, 0, 1)\}.$$

First, note that for any L fixed, (2.1) reads

$$\begin{aligned} \mathbf{F}_{\text{const}}^L(A, B_\varepsilon) = & - \int_{[(0,0,0),(0,1,0)] \times [(0,0,0),(0,0,1)]} \left(\int_{[(1+\varepsilon,0,0),(1+\varepsilon,1,0)] \times [(1+\varepsilon,0,0),(1+\varepsilon,0,1)]} \nabla N(x-y) ds_y \right. \\ & \left. - \int_{[(1+L+\varepsilon,0,0),(1+L+\varepsilon,1,0)] \times [(1+L+\varepsilon,0,0),(1+L+\varepsilon,0,1)]} \nabla N(x-y) ds_y \right) ds_x \\ & - \int_{[(1,0,0),(1,1,0)] \times [(1,0,0),(1,0,1)]} (-1) \left(\int_{[(1+\varepsilon,0,0),(1+\varepsilon,1,0)] \times [(1+\varepsilon,0,0),(1+\varepsilon,0,1)]} \nabla N(x-y) ds_y \right. \\ & \left. - \int_{[(1+L+\varepsilon,0,0),(1+L+\varepsilon,1,0)] \times [(1+L+\varepsilon,0,0),(1+L+\varepsilon,0,1)]} \nabla N(x-y) ds_y \right) ds_x. \end{aligned}$$

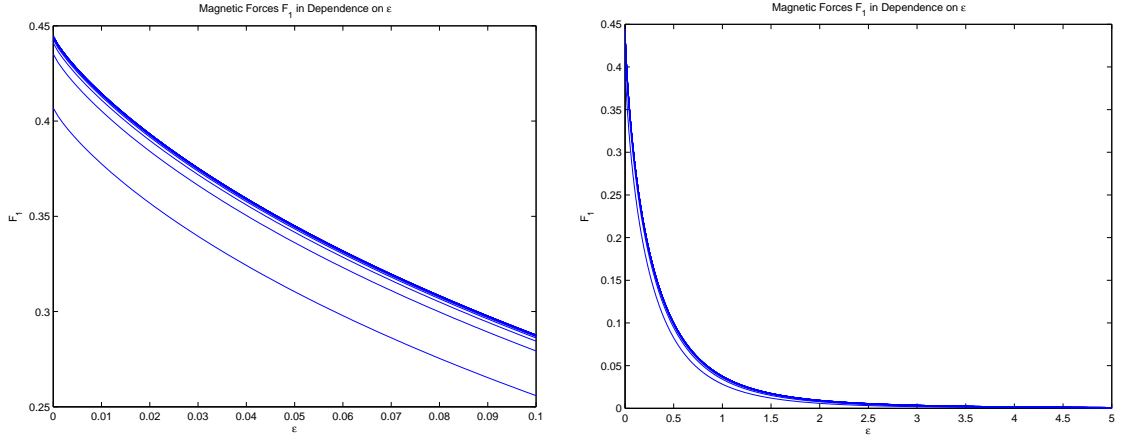
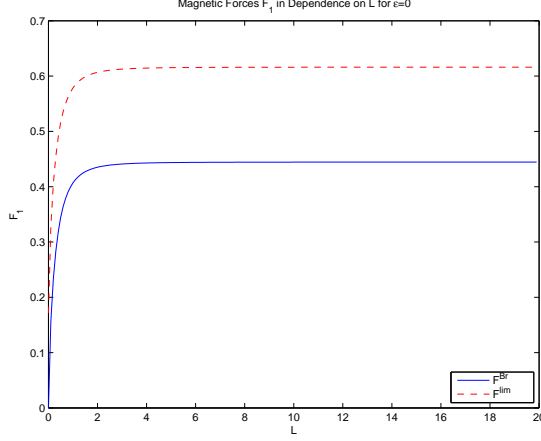


FIGURE 3.7. The force $\mathbf{F}_1(\varepsilon, L)$ in Experiment 1_{3D} in dependence on $\varepsilon \in (0, 0.1]$ (left panel) and $\varepsilon \in (0, 5]$ (right panel). Both panels show curves for varying length $L = 1, \dots, 20$, where $L = 1$ (respectively $L = 20$) corresponds to the lowermost curve (respectively to the uppermost curve). As in Experiment 1_{2D} , we observe (monotone) convergence as $L \rightarrow \infty$.

In Figure 3.7, we plot the first component $\mathbf{F}_1(\varepsilon, L)$ of \mathbf{F} in dependence on the positive distance $\varepsilon > 0$ and the length $L > 0$. As in the two-dimensional case, we observe that the force $\mathbf{F}(\varepsilon, L)$ increases as $\varepsilon \rightarrow 0$, with a finite limit at $\varepsilon = 0$. Moreover, the curves depend in a monotonically increasing fashion on L and converge to a limit curve as $L \rightarrow \infty$. The case when $\varepsilon = 0$ is considered in Figure 3.8, where $\mathbf{F}_1^{\text{Br}}(L)$ and $\mathbf{F}_1^{\text{lim}}(L)$ are plotted in dependence on the length parameter $L > 0$. The surface contribution in Brown's formula (2.2) is given by

$$(3.7) \quad \frac{1}{2} \int_{\partial A \cap \partial B} (\mathbf{m}_A \cdot \mathbf{n}_A)(\mathbf{m}_B \cdot \mathbf{n}_A) \mathbf{n}_A ds_x = \frac{1}{2} |\partial A \cap \partial B| (1, 0, 0).$$

The additional term in the limiting force (2.4) involves the tensor $(S_{ijkp})_{i,j,k,p=1,2,3}$, cf. [PPS, Equation (3.22)]. For the sake of simplicity, we only consider the cubic lattice $\mathcal{L} = \mathbb{Z}^3$ in the following. Then, it can be shown that all elements of $(S_{ijkp})_{i,j,k,p=1,2,3}$ are zero by symmetry except for the



L	\mathbf{F}_1^{Br}	$\mathbf{F}_1^{\text{lim}}$	$\frac{ \mathbf{F}_1^{\text{Br}} - \mathbf{F}_1^{\text{lim}} }{ \mathbf{F}_1^{\text{lim}} }$
1/16	0.116	0.287	59.7%
1/8	0.179	0.351	48.9%
1/4	0.260	0.432	39.7%
1/2	0.345	0.516	33.2%
1	0.407	0.578	29.7%
2	0.435	0.607	28.3%
4	0.443	0.614	27.9%
8	0.444	0.616	27.9%
16	0.445	0.616	27.9%

FIGURE 3.8. The forces \mathbf{F}_1^{Br} (solid) and $\mathbf{F}_1^{\text{lim}}$ (dashed) in Experiment $1_{3\text{D}}$ in dependence on the height L for $\varepsilon = 0$. Analytically, one can show that $\mathbf{F}_1^{\text{lim}}(L) - \mathbf{F}_1^{\text{Br}}(L) = \frac{1}{2}|\partial A \cap \partial B|(S_{1111} - 1) \approx 0.172$ is independent of $L \geq 0$. Moreover, since $\mathbf{F}_1^{\text{Br}}(0^+) = 0$, there holds $\mathbf{F}_1^{\text{lim}}(0^+) > 0$, which implies that the relative error between the two forces tends to 100% for L small. In addition to the graphical illustration (left panel), the table in the right panel gives the numerical values of the forces for certain L -values as well as the deviation with respect to $\mathbf{F}_1^{\text{lim}}$.

terms $S_{iikk} = S_{ikki} = S_{kiki} = -\frac{\mathcal{S}}{2} + \frac{1}{5}$ with $i \neq k$ and $S_{kkkk} = \mathcal{S} + \frac{3}{5}$, where the constant \mathcal{S} is defined by

$$(3.8) \quad \mathcal{S} = -\frac{\gamma}{\pi} \lim_{n \rightarrow \infty} \sum_{z \in \overline{B}_{\frac{n}{2}} \cap \mathcal{L} \setminus \{0\}} \frac{3z_k^2}{|z|^5} \left(3 - 5 \frac{z_k^2}{|z|^2} \right),$$

cf. [Sch05]. In our implementation, we have used the value $\frac{1}{4\pi} 9.33930$ for \mathcal{S} obtained numerically from a brute-force computation. For k fixed, we then obtain

$$\begin{aligned} \sum_{i,j,p=1}^3 S_{ijkp}(\mathbf{m}_A)_i(\mathbf{m}_B)_j(\mathbf{n}_A)_p &= S_{kkkk}(\mathbf{m}_A)_k(\mathbf{m}_B)_k(\mathbf{n}_A)_k \\ &+ S_{iikk} \sum_{\substack{i=1 \\ i \neq k}}^3 \left((\mathbf{m}_A)_i(\mathbf{m}_B)_i(\mathbf{n}_A)_k + (\mathbf{m}_A)_k(\mathbf{m}_B)_i(\mathbf{n}_A)_i + (\mathbf{m}_A)_i(\mathbf{m}_B)_k(\mathbf{n}_A)_i \right). \end{aligned}$$

Taking into account that $(\mathbf{m}_A)_i = \delta_{1i} = (\mathbf{m}_B)_i$ and $(\mathbf{n}_A)_i = \delta_{1i}$ on $\partial A \cap \partial B$, we have

$$\sum_{i,j,p=1}^3 S_{ijkp}(\mathbf{m}_A)_i(\mathbf{m}_B)_j(\mathbf{n}_A)_p = S_{1111}\delta_{1k}.$$


In particular, it follows that the force term coming from the short range effects in the discrete setting only gives a contribution to the first component of the force,

$$\mathbf{F}^{\text{short}} = \frac{1}{2} \sum_{i,j,p=1}^3 (S_{ij1p}, S_{ij2p}, S_{ij3p}) \int_{\partial A \cap \partial B} (\mathbf{m}_A)_i(\mathbf{m}_B)_j(\mathbf{n}_A)_p ds_x = \frac{1}{2}(S_{1111}, 0, 0)|\partial A \cap \partial B|,$$

where $S_{1111} \approx 1.343$. In sum, we have the following expression for the limiting force:

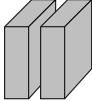
$$(3.9) \quad \mathbf{F}^{\text{lim}} = - \int_{\partial A} (\mathbf{m}_A \cdot \mathbf{n}_A)(x) \oint_{\partial B} (\mathbf{m}_B \cdot \mathbf{n}_B)(y) \nabla N(x-y) ds_y ds_x + \frac{1}{2} |\partial A \cap \partial B| (S_{1111}, 0, 0).$$

Due to (3.7) and (3.9), the difference $\mathbf{F}_1^{\text{lim}}(L) - \mathbf{F}_1^{\text{Br}}(L) = \frac{1}{2} |\partial A \cap \partial B| (S_{1111} - 1)$ is constant for all $L \geq 0$. Moreover, the numerical evidence suggests that $\mathbf{F}_1^{\text{Br}}(L)$ converges to zero as $L \rightarrow 0$, which is also observed in Figure 3.8. Thus, $\mathbf{F}_1^{\text{Br}}(0^+) = 0$ proves that $\mathbf{F}_1^{\text{lim}}(0^+) = \frac{1}{2} (S_{1111} - 1) \approx 0.172$, which is confirmed in Figure 3.8. In particular, the deviation $|\mathbf{F}_1^{\text{Br}} - \mathbf{F}_1^{\text{lim}}|/|\mathbf{F}_1^{\text{lim}}|$ with respect to $\mathbf{F}_1^{\text{lim}}$ tends to 100%. In the limit of $L \rightarrow \infty$, both $\mathbf{F}_1^{\text{Br}}(L)$ and $\mathbf{F}_1^{\text{lim}}(L)$ converge to finite values.

3.2.2. Experiment 2_{3D}.  In this experiment, which is the analog of Experiment 2_{2D}, we consider two equally sized cuboids A and B of varying length $L > 0$,

$$A = \text{conv}\{(0, 0, 0), (0, 1, 0), (0, 1, 1), (0, 0, 1), (L, 0, 0), (L, 1, 0), (L, 1, 1), (L, 0, 1)\} \quad \text{and} \\ B = \text{conv}\{(L, 0, 0), (L, 1, 0), (L, 1, 1), (L, 0, 1), (2L, 0, 0), (2L, 1, 0), (2L, 1, 1), (2L, 0, 1)\}.$$

As in Experiments 1_{2D}, 2_{2D}, and 1_{3D}, the numerical results (not shown) indicate that the force increases with decreasing distance ε and that it converges to a finite value. The curves are monotonically increasing with L and converge to a limit curve as $L \rightarrow \infty$. As in Experiment 1_{3D}, one finds that $\mathbf{F}_1^{\text{lim}}(L) - \mathbf{F}_1^{\text{Br}}(L) = \frac{1}{2} (S_{1111} - 1)$ is independent of $L \geq 0$. Again, one observes numerically that $\mathbf{F}_1^{\text{Br}}(L)$ converges to zero as $L \rightarrow 0$, which implies $\mathbf{F}_1^{\text{lim}}(0^+) = \frac{1}{2} (S_{1111} - 1) \approx 0.172$. Also, the limits of both forces as $L \rightarrow \infty$ are again finite.

3.2.3. Experiment 3_{3D}.  In the third experiment, we assume A and B to be cuboidal and of height and width L :

$$A = \text{conv}\{(0, 0, 0), (0, L, 0), (0, L, L), (0, 0, L), (1, 0, 0), (1, L, 0), (1, L, L), (1, 0, L)\} \quad \text{and} \\ B = \text{conv}\{(1, 0, 0), (1, L, 0), (1, L, L), (1, 0, L), (2, 0, 0), (2, L, 0), (2, L, L), (2, 0, L)\}.$$

Figure 3.9 shows the numerical outcome for positive distances $\varepsilon > 0$. As before, the force increases with decreasing distance $\varepsilon \rightarrow 0$. We also observe monotonicity of the force with L . However, as $L \rightarrow \infty$, no convergence to a limit curve is observed, in contrast to Experiment 3_{2D}, where we did have convergence for $L \rightarrow \infty$. For fixed $\varepsilon > 0$, the force seems to depend linearly on L , since the distance between two curves corresponding to L and $L + 1$, respectively, is constant. Still, one might want to consider Experiment 3_{3D} to be analogous to the two-dimensional Experiment 3_{2D}, in the sense that this effect is presumably only due to the increase in dimension.

In Figure 3.10, we plot the forces \mathbf{F}_1^{Br} and $\mathbf{F}_1^{\text{lim}}$ in dependence on the height and width L . In the limit of $L \rightarrow 0^+$, we observe $\mathbf{F}_1^{\text{Br}}(0^+) = 0 = \mathbf{F}_1^{\text{lim}}(0^+)$. For large values of L , we obtain numerically that \mathbf{F}_1^{Br} increases linearly with L , whereas $\mathbf{F}_1^{\text{lim}}$ increases quadratically. Proceeding as in the derivation of Equations (3.7) and (3.9) above, we obtain that $\mathbf{F}_1^{\text{lim}}(L) - \mathbf{F}_1^{\text{Br}}(L) = \frac{L^2}{2} (S_{1111} - 1)(1, 0, 0)$, which is verified by our numerical data, see e.g. Figure 3.10. The differences to the corresponding plot in Figure 3.4 can probably again be attributed to the increased dimension.

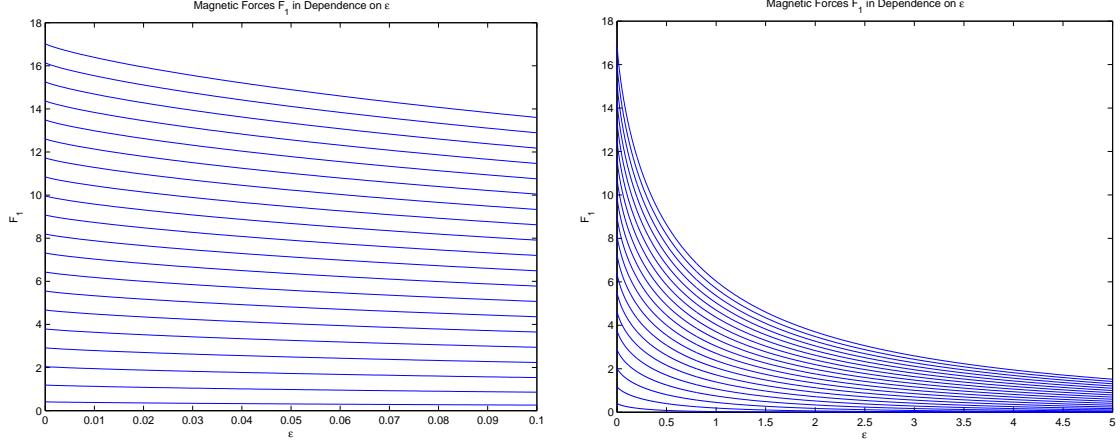


FIGURE 3.9. The force $\mathbf{F}_1(\varepsilon, L)$ in Experiment 3_{3D} in dependence on $\varepsilon \in (0, 0.1]$ (left panel) and $\varepsilon \in (0, 5]$ (right panel). Both panels show curves for varying height $L = 1, \dots, 20$, where $L = 1$ (respectively $L = 20$) corresponds to the downmost curve (respectively to the uppermost curve). We observe a monotone increase of the force as $L \rightarrow \infty$. However, the curves do not converge to a limit curve as $L \rightarrow \infty$.

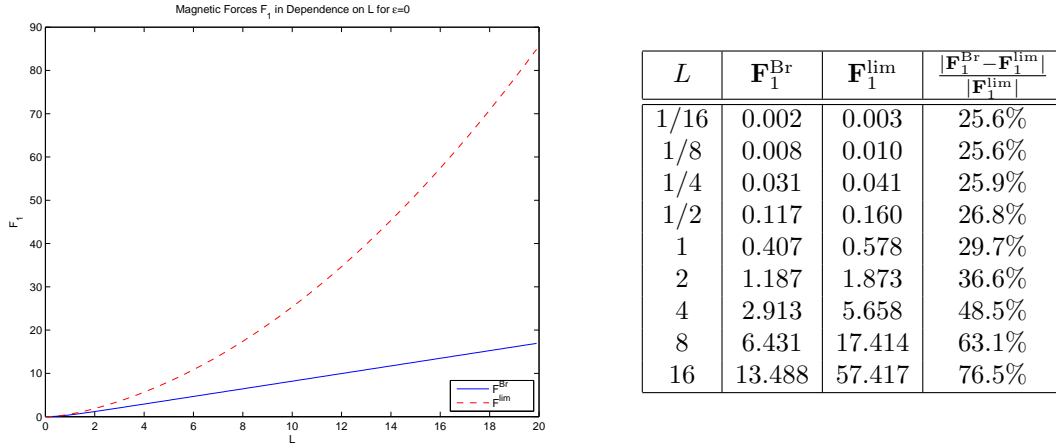


FIGURE 3.10. The forces \mathbf{F}_1^{Br} (solid) and $\mathbf{F}_1^{\text{lim}}$ (dashed) in Experiment 3_{3D} in dependence on L for $\varepsilon = 0$. We observe $\mathbf{F}_1^{\text{lim}}(0^+) = 0 = \mathbf{F}_1^{\text{Br}}(0^+)$. Moreover, $\mathbf{F}_1^{\text{lim}}$ increases quadratically with L , whereas the growth of \mathbf{F}_1^{Br} is merely linear. In addition to the graphical illustration (left panel), the table in the right panel gives the numerical values of the forces for certain L -values as well as the deviation with respect to $\mathbf{F}_1^{\text{lim}}$.



3.2.4. Experiment 4_{3D} .

In the fourth experiment, A and B are defined as two cuboids of equal, varying height, with

$$A = \text{conv}\{(0, 0, 0), (0, 1, 0), (0, 1, L), (0, 0, L), (1, 0, 0), (1, 1, 0), (1, 1, L), (1, 0, L)\} \quad \text{and}$$

$$B = \text{conv}\{(1, 0, 0), (1, 1, 0), (1, 1, L), (1, 0, L), (2, 0, 0), (2, 1, 0), (2, 1, L), (2, 0, L)\}.$$

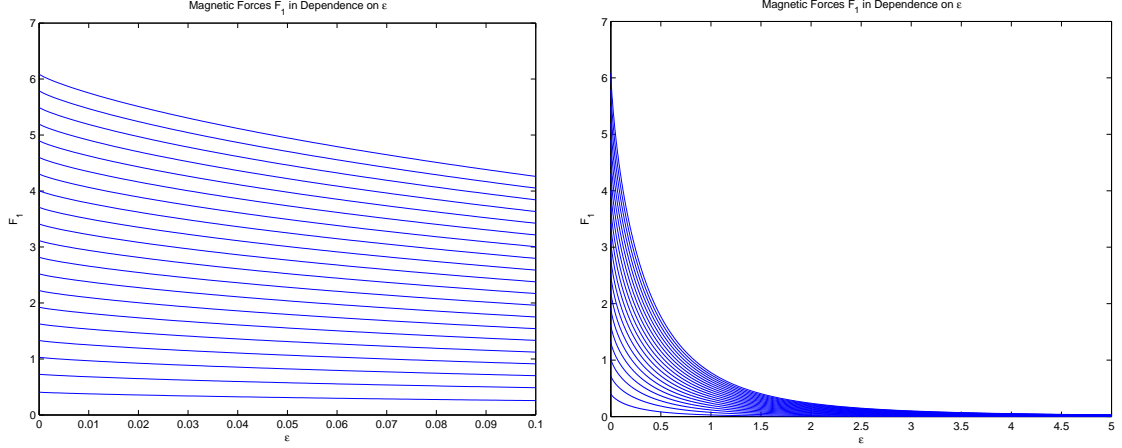
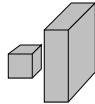


FIGURE 3.11. The force $\mathbf{F}_1(\varepsilon, L)$ in Experiment 4_{3D} in dependence on $\varepsilon \in (0, 0.1]$ (left panel) and $\varepsilon \in (0, 5]$ (right panel). Both panels show curves for varying height $L = 1, \dots, 20$, where $L = 1$ (respectively $L = 20$) corresponds to the downmost curve (respectively to the uppermost curve). We observe a monotone increase of the force as $L \rightarrow \infty$. However, the curves do not converge to a limit curve as $L \rightarrow \infty$.

The numerical outcome for positive distances $\varepsilon > 0$ is similar to that in Experiment 3_{3D} and is shown in Figure 3.11.

For $\varepsilon = 0$, on the other hand, we do not observe the same behavior as in Experiment 3_{3D} , which is due to the different geometries of A and B , cf. Figure 3.12. As $L \rightarrow 0^+$, we still find $\mathbf{F}_1^{\text{Br}}(0^+) = 0 = \mathbf{F}_1^{\text{lim}}(0^+)$. However, the additional term in Brown's formula (3.7) is given by $\frac{L}{2}(1, 0, 0)$ now, and thus is linear in L . Correspondingly, the first component of the short range contribution to $\mathbf{F}_1^{\text{lim}}(L)$ reads $\frac{L}{2}S_{1111} \approx 0.672L$. In sum, we find $\mathbf{F}_1^{\text{lim}}(L) - \mathbf{F}_1^{\text{Br}}(L) = \frac{L}{2}(S_{1111} - 1)(1, 0, 0)$ for the difference between $\mathbf{F}_1^{\text{lim}}$ and \mathbf{F}_1^{Br} , which explains the linear growth of that difference with increasing L , cf. Figure 3.12.



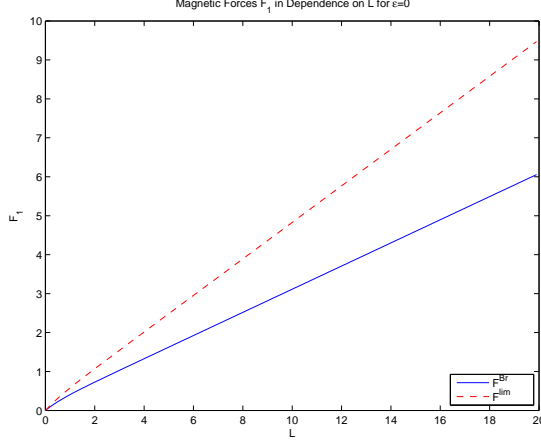
3.2.5. Experiment 5_{3D} .

We assume A to be the cube considered in Experiment 6_{3D} and B to be a cuboid of varying height and depth L ,

$$\begin{aligned}
 A &= \text{conv} \left\{ \left(0, -\frac{1}{2}, -\frac{1}{2}\right), \left(0, \frac{1}{2}, -\frac{1}{2}\right), \left(0, \frac{1}{2}, \frac{1}{2}\right), \left(0, -\frac{1}{2}, \frac{1}{2}\right), \right. \\
 &\quad \left. \left(1, -\frac{1}{2}, -\frac{1}{2}\right), \left(1, \frac{1}{2}, -\frac{1}{2}\right), \left(1, \frac{1}{2}, \frac{1}{2}\right), \left(1, -\frac{1}{2}, \frac{1}{2}\right) \right\} \quad \text{and} \\
 B &= \text{conv} \left\{ \left(1, -\frac{L}{2}, -\frac{L}{2}\right), \left(1, \frac{L}{2}, -\frac{L}{2}\right), \left(1, \frac{L}{2}, \frac{L}{2}\right), \left(1, -\frac{L}{2}, \frac{L}{2}\right), \right. \\
 &\quad \left. \left(2, -\frac{L}{2}, -\frac{L}{2}\right), \left(2, \frac{L}{2}, -\frac{L}{2}\right), \left(2, \frac{L}{2}, \frac{L}{2}\right), \left(2, -\frac{L}{2}, \frac{L}{2}\right) \right\},
 \end{aligned}$$

where the geometry of B is again symmetric with respect to A , and the surface measure of $\partial A \cap \partial B$ is $\min\{1, L^2\}$ now.

Note that this experiment is equivalent to Experiment 4_{2D} in the sense that we obtain a similar qualitative behavior, cf. Figures 3.5 and 3.13. Again, the force $\mathbf{F}(\varepsilon, L)$ converges pointwise to zero as $L \rightarrow \infty$, whereas we do not observe monotone convergence. Figure 3.14 shows $\mathbf{F}_1^{\text{Br}}(L)$ and $\mathbf{F}_1^{\text{lim}}(L)$ for $\varepsilon = 0$. On numerical grounds we infer that both forces satisfy $\mathbf{F}_1^{\text{Br}}(0^+) = 0 = \mathbf{F}_1^{\text{lim}}(0^+)$.



L	\mathbf{F}_1^{Br}	$\mathbf{F}_1^{\text{lim}}$	$\frac{ \mathbf{F}_1^{\text{Br}} - \mathbf{F}_1^{\text{lim}} }{ \mathbf{F}_1^{\text{lim}} }$
1/16	0.031	0.042	25.8%
1/8	0.061	0.082	26.1%
1/4	0.118	0.161	26.7%
1/2	0.223	0.309	27.8%
1	0.407	0.578	29.7%
2	0.727	1.070	32.1%
4	1.329	2.015	34.1%
8	2.519	3.891	35.3%
16	4.896	7.642	35.9%

FIGURE 3.12. The forces \mathbf{F}_1^{Br} (solid) and $\mathbf{F}_1^{\text{lim}}$ (dashed) in Experiment 4_{3D} in dependence on L for $\varepsilon = 0$. We observe $\mathbf{F}_1^{\text{lim}}(0^+) = 0 = \mathbf{F}_1^{\text{Br}}(0^+)$ as well as a linear dependence of both forces on L . As expected, $\mathbf{F}_1^{\text{lim}}$ and \mathbf{F}_1^{Br} increase linearly with L , with slopes 0.5 and 0.672, respectively. In addition to the graphical illustration (left panel), the table in the right panel gives the numerical values of the forces for certain L -values as well as the deviation with respect to $\mathbf{F}_1^{\text{lim}}$.

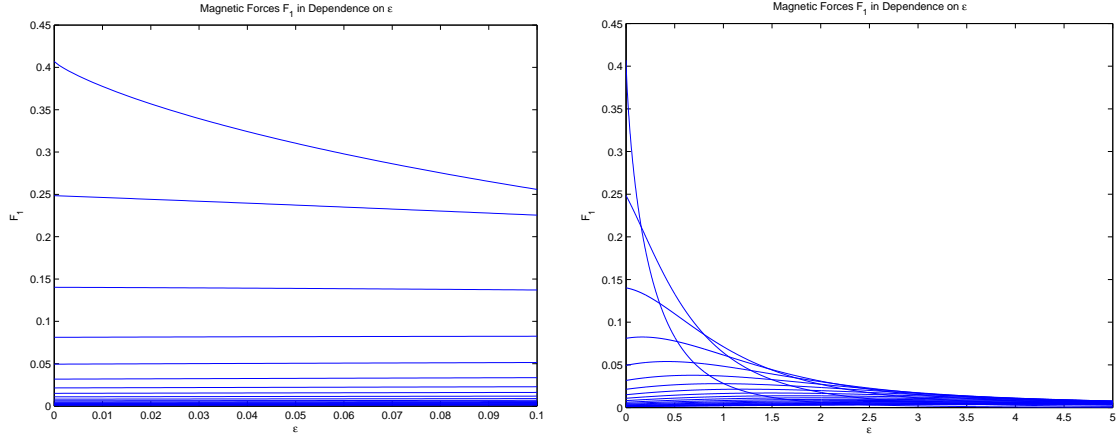
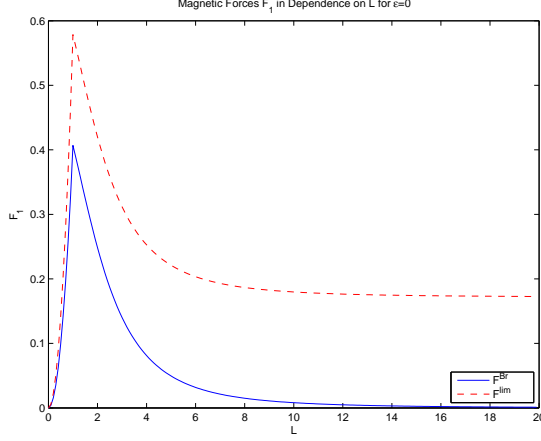


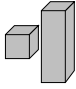
FIGURE 3.13. The force $\mathbf{F}_1(\varepsilon, L)$ in Experiment 5_{3D} in dependence on $\varepsilon \in (0, 0.1]$ (left panel) and $\varepsilon \in (0, 5]$ (right panel). Both panels show curves for varying height/depth $L = 1, \dots, 20$, where $L = 1$ (respectively $L = 20$) corresponds to the uppermost curve (respectively to the downmost curve) for ε small (left panel). We observe pointwise convergence to zero as $L \rightarrow \infty$. However, the convergence is not monotone in L for ε fixed (right panel).

Moreover, their difference is given by $\mathbf{F}_1^{\text{lim}}(L) - \mathbf{F}_1^{\text{Br}}(L) = \frac{1}{2} \min\{1, L^2\}(S_{1111} - 1) \approx 0.172 \min\{1, L^2\}$ for all L and is therefore constant for $L \geq 1$. For $L \rightarrow \infty$, we find $\mathbf{F}_1^{\text{Br}}(\infty) = 0$ and consequently $\mathbf{F}_1^{\text{lim}}(\infty) \approx 0.172$. In particular, this implies that in the large- L regime, i.e., for the force acting between two large parallel plates, Brown's formula predicts a vanishing force, whereas $\mathbf{F}_1^{\text{lim}}$ gives an attracting contribution.



L	\mathbf{F}_1^{Br}	$\mathbf{F}_1^{\text{lim}}$	$\frac{ \mathbf{F}_1^{\text{Br}} - \mathbf{F}_1^{\text{lim}} }{ \mathbf{F}_1^{\text{lim}} }$
1/16	0.002	0.002	30.5%
1/8	0.006	0.009	30.5%
1/4	0.024	0.035	30.5%
1/2	0.099	0.142	30.3%
1	0.407	0.578	29.7%
2	0.248	0.420	40.8%
4	0.081	0.253	67.9%
8	0.015	0.187	92.0%
16	0.002	0.174	98.8%

FIGURE 3.14. The forces \mathbf{F}_1^{Br} (solid) and $\mathbf{F}_1^{\text{lim}}$ (dashed) in Experiment $5_{3\text{D}}$ in dependence on L for $\varepsilon = 0$. We observe $\mathbf{F}_1^{\text{Br}}(0^+) = 0 = \mathbf{F}_1^{\text{lim}}(0^+)$. For $L \geq 1$, the difference $\mathbf{F}_1^{\text{lim}}(L) - \mathbf{F}_1^{\text{Br}}(L) = \frac{1}{2}(S_{1111} - 1) \approx 0.172$ is constant, where $\mathbf{F}_1^{\text{Br}}(\infty) = 0$ and $\mathbf{F}_1^{\text{lim}}(\infty) \approx 0.172$. In addition to the graphical illustration (left panel), the table in the right panel gives the numerical values of the forces for certain L -values as well as the deviation with respect to $\mathbf{F}_1^{\text{lim}}$.

3.2.6. Experiment $6_{3\text{D}}$.  We assume A to be a cube and B to be a cuboid of varying height L ,

$$\begin{aligned}
A &= \text{conv} \left\{ \left(0, -\frac{1}{2}, -\frac{1}{2}\right), \left(0, \frac{1}{2}, -\frac{1}{2}\right), \left(0, \frac{1}{2}, \frac{1}{2}\right), \left(0, -\frac{1}{2}, \frac{1}{2}\right), \right. \\
&\quad \left. \left(1, -\frac{1}{2}, -\frac{1}{2}\right), \left(1, \frac{1}{2}, -\frac{1}{2}\right), \left(1, \frac{1}{2}, \frac{1}{2}\right), \left(1, -\frac{1}{2}, \frac{1}{2}\right) \right\} \quad \text{and} \\
B &= \text{conv} \left\{ \left(1, -\frac{1}{2}, -\frac{L}{2}\right), \left(1, \frac{1}{2}, -\frac{L}{2}\right), \left(1, \frac{1}{2}, \frac{L}{2}\right), \left(1, -\frac{1}{2}, \frac{L}{2}\right), \right. \\
&\quad \left. \left(2, -\frac{1}{2}, -\frac{L}{2}\right), \left(2, \frac{1}{2}, -\frac{L}{2}\right), \left(2, \frac{1}{2}, \frac{L}{2}\right), \left(2, -\frac{1}{2}, \frac{L}{2}\right) \right\},
\end{aligned}$$

i.e., the geometry of B is symmetric with respect to A .

The surface measure of $\partial A \cap \partial B$ is $\min\{1, L\}$ and is therefore non-smooth in L . Note, however, that this experiment is not analogous to Experiment $4_{2\text{D}}$: Contrary to Experiment $5_{3\text{D}}$ above, the force does not converge pointwise to zero as $L \rightarrow \infty$, but to a positive limit curve (not shown).

Apart from this difference, we do observe several similarities to Experiment $5_{3\text{D}}$: According to the numerics, the convergence again seems to be monotone decreasing with L for $\varepsilon \in (0, 0.1]$, whereas it is non-monotone in the full range of $\varepsilon \in (0, 5]$. Moreover, for $\varepsilon = 0$, we observe $\mathbf{F}_1^{\text{Br}}(0^+) = 0 = \mathbf{F}_1^{\text{lim}}(0^+)$. Both $\mathbf{F}_1^{\text{Br}}(L)$ and $\mathbf{F}_1^{\text{lim}}(L)$ have a global maximum at $L = 1$, where the dependence on L is non-differentiable. Analytically, we obtain $\mathbf{F}_1^{\text{lim}}(L) - \mathbf{F}_1^{\text{Br}}(L) = \frac{1}{2} \min\{1, L\}(S_{1111} - 1)$, i.e., the difference between the two forces does not depend on L for $L \geq 1$. Therefore, the distance between the corresponding curves has to be constant if $L \geq 1$, which is in fact observed numerically. For $L \rightarrow \infty$, both $\mathbf{F}_1^{\text{Br}}(L)$ and $\mathbf{F}_1^{\text{lim}}(L)$ converge to positive values.

3.2.7. Experiment 7_{3D}.



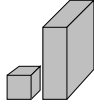
We assume A to be a cube, as defined in Experiment 1_{3D}, and B to be a cuboid of varying height L and depth 1, where both A and B are anchored at the origin for all L :

$$A = \text{conv}\{(0, 0, 0), (0, 1, 0), (0, 1, 1), (0, 0, 1), (1, 0, 0), (1, 1, 0), (1, 1, 1), (1, 0, 1)\} \quad \text{and}$$

$$B = \text{conv}\{(1, 0, 0), (1, 1, 0), (1, 1, 1), (1, 0, 1), (2, 0, 0), (2, 1, 0), (2, 1, L), (2, 0, L)\}.$$

Numerically, we observe convergence of the curves to a positive limit curve for $L \rightarrow \infty$ (not shown). However, as in the previous experiment, the convergence is non-monotone in L in the full ε -range under consideration. The curves are monotonically increasing for $\varepsilon \rightarrow 0$, with $\mathbf{F}_1(0^+, L)$ finite. Numerically, one finds that both $\mathbf{F}_1^{\text{Br}}(L)$ and $\mathbf{F}_1^{\text{lim}}(L)$ attain a non-differentiable, global maximum at $L = 1$. As $L \rightarrow 0^+$, both curves are strictly decreasing, with $\mathbf{F}_1^{\text{Br}}(0^+) = 0 = \mathbf{F}_1^{\text{lim}}(0^+)$. Moreover, as $L \rightarrow \infty$, both forces tend to positive finite values $\mathbf{F}_1^{\text{Br}}(\infty)$ and $\mathbf{F}_1^{\text{lim}}(\infty)$, respectively. For the difference between \mathbf{F}_1^{Br} and $\mathbf{F}_1^{\text{lim}}$, one finds $\mathbf{F}_1^{\text{lim}}(L) - \mathbf{F}_1^{\text{Br}}(L) = \frac{1}{2} \min\{1, L\}(S_{1111} - 1) \approx 0.172 \min\{1, L\}$, which is constant for $L \geq 1$, in agreement with the numerical outcome (not shown).

3.2.8. Experiment 8_{3D}.



Finally, we take A to be the cube considered in Experiment 1_{3D} and B to be a cuboid of varying height and depth L , where A and B again share a common corner for all L :

$$A = \text{conv}\{(0, 0, 0), (0, 1, 0), (0, 1, 1), (0, 0, 1), (1, 0, 0), (1, 1, 0), (1, 1, 1), (1, 0, 1)\} \quad \text{and}$$

$$B = \text{conv}\{(1, 0, 0), (1, L, 0), (1, L, L), (1, 0, L), (2, 0, 0), (2, L, 0), (2, L, L), (2, 0, L)\}.$$

Note that this experiment is equivalent to Experiment 5_{2D} in two dimensions, in the sense that we observe the same qualitative behavior. Moreover, the numerical outcome (not shown) is analogous to that of Experiment 7_{3D}; in fact, the only variation is that $\mathbf{F}_1^{\text{lim}}(L) - \mathbf{F}_1^{\text{Br}}(L) = \frac{1}{2} \min\{1, L^2\}(S_{1111} - 1)$ now, i.e., the difference between $\mathbf{F}_1^{\text{lim}}$ and \mathbf{F}_1^{Br} decays quadratically with L for L small. Hence, we refer to the discussion of Experiment 7_{3D} above for details.

4. CONCLUSIONS AND OUTLOOK

In this article as well as in the accompanying Part I [PPS], we have analyzed and compared several formulae which have been proposed in the literature to describe the magnetic force between macroscopic rigid bodies in two and three space dimensions. The aim of our analysis has been to obtain a better understanding of the different force formulae that are available in the literature. In fact, the eventual goal is to understand which of these formulae is the most appropriate one to model the magnetic force within magnetized rigid bodies. Since it seems impossible to measure magnetic forces acting on a portion of a body directly, the idea underlying our approach has been to study the magnetic force between two separated bodies in dependence on their mutual distance, as well as the force when the bodies are brought into contact.

More specifically, we have proceeded as follows: In case the two bodies, which we denote by A and B , are a positive distance ε apart, we have considered a classical force formula \mathbf{F} . Secondly, we have analytically proven two formulae for A and B in contact, i.e., for $\varepsilon = 0$: \mathbf{F}^{Br} (from macroscopic electrodynamics) and \mathbf{F}^{lim} (via a multiscale approach), under quite general assumptions on the regularity of A and B as well as on the corresponding magnetizations.

In the present, second part of our study, we have investigated these formulae in a series of numerical experiments under the additional assumption that the underlying lattice is square in \mathbb{R}^2 and cubic in \mathbb{R}^3 , respectively. To further simplify the numerical analysis in Section 3, the magnets

A and B are assumed to be of polygonal (rectangular or cuboidal) shape, and the magnetization is chosen to be constant on A and B , respectively. More precisely, we set $\mathbf{m}_A = \mathbf{m}_B$. (As pointed out in [PPS, Remark 3.6(a)], for $\mathbf{m}_A = -\mathbf{m}_B$, the values of the forces are simply multiplied by -1 . In general, if $\mathbf{m}_A = \mu\mathbf{m}_B$ for some $\mu \in \mathbb{R}$, the corresponding force terms have to be multiplied by μ , cf. also Equations (2.1)–(2.4).)

The goal of these experiments has been to provide numerical data that can be compared with data from corresponding real-life experiments, which we leave to the experimentalists [Eim06]. Our hope is that these real-life experiments in combination with our numerical results will help to clarify the question which force formula is the correct one for $\varepsilon = 0$, in the sense that it describes nature most accurately. Here, it is important to note that the classical force formula \mathbf{F} has, to the best of our knowledge, only been verified experimentally if the distance between A and B is large. Whether that formula still applies as the distance between the two bodies tends to zero is one of the questions addressed in our study. If \mathbf{F}^{Br} turns out to be the appropriate formula for $\varepsilon = 0$, \mathbf{F} will provide a good approximation, since $\lim_{\varepsilon \rightarrow 0} \mathbf{F} = \mathbf{F}^{\text{Br}}$, cf. [PPS]. If, however, \mathbf{F}^{lim} reflects the experimental data better, \mathbf{F} will certainly not be appropriate for small ε : From a physical point of view, we expect the (measured) magnetic force to be continuous as $\varepsilon \rightarrow 0$, whereas the additional contribution to \mathbf{F}^{lim} due to $\mathbf{F}^{\text{short}}$ introduces a discontinuity at $\varepsilon = 0$. Intuitively speaking, similar contributions should already occur for ε small but positive, and the resulting limiting formulae should depend continuously on ε . For a related study that will hopefully lead to a better understanding of the relation between \mathbf{F} and \mathbf{F}^{lim} , we refer the reader to [SS07], where a transition between the two is derived via a multi-scale approach.

We first summarize a few of our findings in more detail: Without exception, the numerical experiments in Section 3 show that the magnetic force \mathbf{F} acting between two bodies A and B which are a distance ε apart and equally magnetized increases with decreasing ε , as expected. Moreover, \mathbf{F} is non-repelling and finite for any choice of $\varepsilon > 0$. In particular, the limit of \mathbf{F} as $\varepsilon \rightarrow 0$ is finite, as well, and equals the value predicted by Brown’s force formula \mathbf{F}^{Br} , see [PPS, Section 3.1] for an analytical demonstration. Similarly, we find that the second formula for $\varepsilon = 0$ considered in [PPS], \mathbf{F}^{lim} , also gives a finite non-repelling contribution throughout. As for the difference between \mathbf{F}^{Br} and \mathbf{F}^{lim} , we can basically distinguish three cases:

- (i) The difference $\mathbf{F}^{\text{lim}} - \mathbf{F}^{\text{Br}}$ is constant, i.e., independent of the geometry parameter L , as for instance in Experiments 1_{2D} and 1_{3D}.
- (ii) Similarly to (i), $\mathbf{F}^{\text{lim}} - \mathbf{F}^{\text{Br}}$ is constant when $L \geq 1$; however, it scales linearly or quadratically in L if $L < 1$, cf. Experiments 4_{2D} and 6_{3D} or Experiment 8_{3D}.
- (iii) The dependence of $\mathbf{F}^{\text{lim}} - \mathbf{F}^{\text{Br}}$ on L is linear or quadratic throughout, as is the case in Experiments 3_{2D} and 4_{3D} or in Experiment 3_{3D}, respectively.

Furthermore, we note that in some of our experiments, Brown’s force formula gives a vanishing contribution for large values of L , whereas the contribution coming from \mathbf{F}^{lim} is still attracting, see e.g. Experiments 4_{2D} or 7_{3D}. Interestingly, this implies that, at least in the setting of Section 3, the remainder $\mathbf{F}^{\text{long}} = \mathbf{F}^{\text{lim}} - \mathbf{F}^{\text{short}}$ cannot be an admissible force formula by its own: Indeed, by formula (2.3), it follows that for $\mathbf{F}_1^{\text{Br}} = 0$, $\mathbf{F}_1^{\text{long}}(A, B) = -\frac{1}{2}|\partial A \cap \partial B| < 0$. However, this contradicts what one would expect on physical grounds, since the force cannot be repelling if $\mathbf{m}_A = \mathbf{m}_B$ as in Section 3.

Based on our observations, we suggest to investigate the following experiments in a real-life setup. Experiments 1_{3D} as well as 2_{3D} seem preferable for testing \mathbf{F} in the entire range of $\varepsilon > 0$. These two experiments might also be useful for calibrating the measured data with our numerical results. (Recall that we set $\gamma = 1$ and $|\mathbf{m}_A| = |\mathbf{m}_B| = 1$ and that, moreover, we have not fixed a length scale.) The calibration should be done for ε large, since the classical formula \mathbf{F} is widely believed to hold true in that regime. When $\varepsilon = 0$, the numerical values of \mathbf{F}_1^{Br} and $\mathbf{F}_1^{\text{lim}}$ in both

Experiments 1_{3D} and 2_{3D} differ by a fixed constant. The deviation with respect to $\mathbf{F}_1^{\text{lim}}$ is quite large; it equals for instance 29.7% if both bodies A and B are unit cubes, cf. Figure 3.8. Therefore, it should be detectable in measurements.

Real-life experiments corresponding to Experiment 3_{3D}, on the other hand, seem particularly useful if they are performed for different values of L and $\varepsilon \approx 0$. Since \mathbf{F}^{lim} increases quadratically with L for large values of L , whereas \mathbf{F}^{Br} increases linearly, this setup should give some insight into whether \mathbf{F}^{Br} or \mathbf{F}^{lim} describes the measured force better. Recall that the difference $\mathbf{F}^{\text{lim}} - \mathbf{F}^{\text{Br}}$ is quadratic in L . Hence, the deviation with respect to \mathbf{F}^{lim} grows considerably with L , and is e.g. already 76% for $L = 16$, cf. Figure 3.10.

Experiment 5_{3D} can be interpreted in a similar fashion if L is smaller than 1, since $\mathbf{F}^{\text{lim}} - \mathbf{F}^{\text{Br}}$ depends quadratically on L in that case. Moreover, our numerical analysis predicts that \mathbf{F}^{Br} is zero for large L , whereas \mathbf{F}^{lim} converges to a finite value. In other words, Brown’s formula predicts that there is no force acting between two equally magnetized bodies of which one is a large plate and the other one is a relatively small cube centered at one face of the plate; the limiting formula, however, gives an attracting force. It would be interesting to clarify these observations experimentally.

Preliminary real-life experimental results obtained by T. Eimüller and his group [Eim06] indicate that the measured magnetic forces are in good agreement with the classical force formula \mathbf{F} if ε is large. However, as ε tends to zero, the measured values deviate from the ones computed from \mathbf{F} . Since the measured forces are as strong as some tens of N, the observed deviation is certainly not due to so-called van-der-Waals or Casimir forces, which indicates that the magnetic force formulae studied in this article might well play a role here. Further experimental studies are in progress and will be published elsewhere.

Next, we briefly comment on some limitations of the present work, as well as on possible generalizations. A first natural generalization is to drop the assumption of uniform magnetizations. It is well-known from micromagnetic theory that the energy-minimizing magnetization in a polygonal magnetic body is not uniform, see e.g. [HS98, DKMO06]. In particular, the energy-minimizing magnetization might depend on the distance between the bodies. However, if the material under consideration is a hard permanent magnet, the assumption of a uniform magnetization seems reasonable if the size of the samples is sufficiently large. A generalization to non-constant magnetizations is already included in the analysis of [PPS, Sections 2 and 3]; however, it makes the numerical implementation considerably more complicated and is therefore postponed to a future article.

Furthermore, for the computation of the limiting force \mathbf{F}^{lim} in the framework of Section 3, we have always assumed that the underlying lattice structure is described by \mathbb{Z}^2 and \mathbb{Z}^3 , respectively. Other choices of Bravais lattices can be treated analogously; one only has to compute the tensor $(S_{ijkp})_{i,j,k,p=1,\dots,d}$ accordingly. Here methods from number theory might be useful, see [Sch05, p. 264] for more details. Similar considerations in the context of polycrystalline materials, which are of special interest with respect to applications, are still an open topic.

Another issue could be our assumption that the boundaries are flat; that is, we neglect any small scratches which might result from polishing the magnets. Analytical methods for proving such force formulae for non-flat boundaries are known, but they do not apply in the case of infinitely many “wiggles,” cf. [Sch05, p. 261]. Still, the numerical values of the force computed from the different force formulae vary considerably for $\varepsilon = 0$, see Section 3. Hence, we believe that these differences can be reproduced in real-life experiments with large hard permanent magnets that are well polished. Note that this restriction to large magnetized bodies is only due to our assumption that the magnetizations are uniform. Otherwise, we impose no limitation on the size of the bodies, neither in [PPS] nor in the present article. To state it differently, our analytical results are, in principle, applicable to bodies ranging from a nanoscale to a macroscopic scale.

Finally, an additional, largely open topic is the question if, and how, the present analysis carries over from rigid to deformable magnetized bodies. A clarifying answer is of interest, for instance, in the context of moving interfaces in ferromagnetic shape-memory alloys [Jam02].

These and similar questions will be the topic of future research.

Acknowledgment. AS thanks P. Bruno for a fruitful discussion that stimulated the study of Experiment 4_{2D}, which in turn influenced the selection of further numerical experiments as well as the conclusions. NP is grateful to C.E. Wayne for helpful discussions and insightful comments on the convergence of the integrals occurring in Section 2. The research of NP was supported partly by the Austrian Science Fund FWF under grant P15274 and partly by the U.S. National Science Foundation under grant DMS-0109427. Part of this work was performed while AS was affiliated with the Institute of Analysis, Dynamics, and Modeling at the University of Stuttgart. Moreover, AS was supported by the RTN network MRTN-CT-2004-50522.

APPENDIX A. SOME IMPLEMENTATIONAL DETAILS

1.1. The Two-Dimensional Case. For the convenience of the reader, we briefly indicate how the single-layer potential \mathcal{S} as well as the antiderivative \mathcal{F} introduced in Section 2.1 can be evaluated.

Regarding the computation of \mathcal{S} , we cite a relevant result from [Car01] here; similar formulae can be found in [Mai99, Pra03].

Lemma A.1 ([Car01, p. 47]). *For $x, a, b \in \mathbb{R}^2$, let $[a, b] = \text{conv}\{a, b\}$. Moreover, define $c = (b + a) - 2x$ and $d = b - a$ as well as*

$$z = \frac{(d_1 c_1 + d_2 c_2) \pm i |d_1 c_2 - d_2 c_1|}{d_1^2 + d_2^2} \in \mathbb{C}.$$

Then, there holds

$$\begin{aligned} & \int_{[a,b]} \log |x - y| ds_y \\ &= \frac{|d|}{2} \left(2 \left(\log \frac{|d|}{2} - 1 \right) + \Re[(1 - z) \log_{\mathbb{C}}(1 - z)] + \Re[(1 + z) \log_{\mathbb{C}}(-1 - z)] \right), \end{aligned}$$

where $\log_{\mathbb{C}}$ is the complex logarithm and \Re denotes the real part.

A formula for \mathcal{F} in (2.8) can be obtained directly as follows:

Lemma A.2. *For $x_2 - y_2 \neq 0$, there holds*

$$(A.1) \quad \mathcal{F}(x_1, y_1; x_2 - y_2) = -(x_1 - y_1) \arctan \frac{x_1 - y_1}{x_2 - y_2} + (x_2 - y_2) \log |x - y|.$$

Remark A.1. For $x_2 - y_2 = 0$, \mathcal{F} is obviously zero by definition. □

1.2. The Three-Dimensional Case. Next, we summarize the analytical formulae from [Mai00] required for the computation of the quantities $F_{0000}^{-3/2}$, $G_{000}^{-1/2}$, and $\mathcal{G}_{000}^{-1/2}$, cf. Section 2.2. The computation is done recursively and is based on the evaluation of the more elementary antiderivatives

$$(A.2) \quad \begin{aligned} g_k^p(y; x, a) &:= \int y^k \{(y - x)^2 + a^2\}^p dy, \\ G_{k\ell}^p(y_1, y_2; x_1, x_2, a) &:= \int \int y_1^k y_2^\ell \{(y_1 - x_1)^2 + (y_2 - x_2)^2 + a^2\}^p dy_2 dy_1, \end{aligned}$$

as is shown in the following lemmas. We only cite the results for the values of k and p occurring in our analysis. For the general formulae we refer to [Mai00].

Lemma A.3 ([Mai00, Equations (13) and (10)]). *Given $a \neq 0$, there holds*

$$g_0^{-1/2}(y; x, a) = \operatorname{arsinh} \frac{y-x}{|a|},$$

$$g_1^{-1/2}(y; x, a) = \{(y-x)^2 + a^2\}^{1/2} + xg_0^{-1/2}(y; x, a).$$

□

Lemma A.4 ([Mai00, Equations (17), (18), and (14)]). *Given $a \neq 0$, $G_{00}^{-3/2}$ and $G_{01}^{-3/2}$ can be written as*

$$G_{00}^{-3/2}(y_1, y_2; x_1, x_2, a) = \frac{\operatorname{sign}\{(y_1 - x_1)(y_2 - x_2)a\}}{2a}$$

$$\times \arccos \left(\frac{-2(y_1 - x_1)^2(y_2 - x_2)^2}{\{(y_1 - x_1)^2 + a^2\}\{(y_2 - x_2)^2 + a^2\}} + 1 \right)$$

and

$$G_{01}^{-3/2}(y_1, y_2; x_1, x_2, a) = -\operatorname{arsinh} \frac{y_1 - x_1}{\{(y_2 - x_2)^2 + a^2\}^{1/2}} + x_2 G_{00}^{-3/2}(y_1, y_2; x_1, x_2, a),$$

respectively. For $a \in \mathbb{R}$ arbitrary, one has the following recurrence formulae for $G_{00}^{-1/2}$ and $G_{01}^{-1/2}$:

$$G_{00}^{-1/2}(y_1, y_2; x_1, x_2, a) = (y_1 - x_1) g_0^{-1/2}(y_2; x_2, \{(y_1 - x_1)^2 + a^2\}^{1/2})$$

$$+ (y_2 - x_2) g_0^{-1/2}(y_1; x_1, \{(y_2 - x_2)^2 + a^2\}^{1/2})$$

$$- a^2 G_{00}^{-3/2}(y_1, y_2; x_1, x_2, a),$$

$$G_{01}^{-1/2}(y_1, y_2; x_1, x_2, a) = \frac{1}{2}(y_1 - x_1) g_1^{-1/2}(y_2; x_2, \{(y_1 - x_1)^2 + a^2\}^{1/2})$$

$$+ \frac{1}{2}y_2(y_2 - x_2) g_0^{-1/2}(y_1; x_1, \{(y_2 - x_2)^2 + a^2\}^{1/2})$$

$$+ \frac{1}{2}x_2 G_{00}^{-1/2}(y_1, y_2; x_1, x_2, a) - \frac{1}{2}a^2 G_{01}^{-3/2}(y_1, y_2; x_1, x_2, a).$$

□

Finally, we state the corresponding closed-form formulae for the antiderivatives in (2.22)–(2.24) which are used in the computation of D_j^{\parallel} and D_j^{\perp} :

Lemma A.5 ([Mai00, Equations (40), (21), and (25)]). *The antiderivatives $F_{0000}^{-3/2}$, $G_{000}^{-1/2}$, and $\mathcal{G}_{000}^{-1/2}$ in (2.22)–(2.24) read*

$$F_{0000}^{-3/2}(x_1, x_2, y_1, y_2; x_3 - y_3) = (x_1 - y_1)(x_2 - y_2) G_{00}^{-3/2}(x_1, x_2; y_1, y_2, x_3 - y_3)$$

$$+ (x_1 - y_1) g_0^{-1/2}(x_1; y_1, \{(x_2 - y_2)^2 + (x_3 - y_3)^2\}^{1/2})$$

$$+ (x_2 - y_2) g_0^{-1/2}(x_2; y_2, \{(x_1 - y_1)^2 + (x_3 - y_3)^2\}^{1/2})$$

$$- |x - y|,$$

$$G_{000}^{-1/2}(y_1, y_2, y_3; x_1, x_2, x_3) = \frac{1}{2}(y_1 - x_1) G_{00}^{-1/2}(y_2, y_3; x_2, x_3, y_1 - x_1)$$

$$+ \frac{1}{2}(y_2 - x_2) G_{00}^{-1/2}(y_1, y_3; x_1, x_3, y_2 - x_2)$$

$$+ \frac{1}{2}(y_3 - x_3) G_{00}^{-1/2}(y_1, y_2; x_1, x_2, y_3 - x_3),$$

and

$$\mathcal{G}_{000}^{-1/2}(x_2, y_1, y_2; x_1, x_3 - y_3) = y_2 \mathcal{G}_{00}^{-1/2}(y_1, x_2; x_1, y_2, x_3 - y_3) + G_{01}^{-1/2}(y_1, y_2; x_1, x_2, x_3 - y_3),$$

respectively. \square

APPENDIX B. ANALYSIS OF THE FORCES FOR $d = 2$

We conclude the appendix by showing how the integral of ∇N can be computed explicitly for $d = 2$. The following result is useful for the qualitative analysis of the expressions obtained for $\mathbf{F}(\varepsilon, L)$ in the context of the numerical experiments of Section 3:

Lemma B.1. *Let $d = 2$, and let $E = \{x_1\} \times [a_2, b_2]$ and $\tilde{E} = \{y_1\} \times [c_2, d_2]$ denote vertical line segments of height $h = b_2 - a_2$ and $\tilde{h} = d_2 - c_2$, respectively. Moreover, assume $x_1 \neq y_1$, and let $s = y_1 - x_1 \in \mathbb{R} \setminus \{0\}$. Then, there holds*

$$\begin{aligned} I^{h, \tilde{h}}(s) &:= \int_E \int_{\tilde{E}} \nabla N(x - y) ds_y ds_x \\ &= \frac{1}{2\pi} \left(-(\tilde{h} - h) \arctan \frac{\tilde{h} - h}{s} + \frac{s}{2} \ln \left(1 + \frac{(\tilde{h} - h)^2}{s^2} \right) + h \arctan \frac{h}{s} \right. \\ &\quad \left. - \frac{s}{2} \ln \left(1 + \frac{h^2}{s^2} \right) + \tilde{h} \arctan \frac{\tilde{h}}{s} - \frac{s}{2} \ln \left(1 + \frac{\tilde{h}^2}{s^2} \right), 0 \right)^T. \end{aligned}$$

Proof. With s defined as above, a parameterization of the curves via $x = (x_1, t)$ and $y = (y_1, t')$ yields

$$\begin{aligned} I^{h, \tilde{h}}(s) &= \left(\frac{s}{2\pi} \int_0^h \int_0^{\tilde{h}} \frac{1}{s^2 + (t - t')^2} dt dt', 0 \right)^T = \left(\frac{s}{2\pi} \int_0^h \left[\frac{1}{s} \arctan \frac{t - t'}{s} \right]_{t=0}^{\tilde{h}} dt', 0 \right)^T \\ &= \left(\frac{1}{2\pi} \int_0^h \left(\arctan \frac{\tilde{h} - t'}{s} - \arctan \frac{-t'}{s} \right) dt', 0 \right)^T \\ &= \frac{1}{2\pi} \left(\left[(t' - \tilde{h}) \arctan \frac{\tilde{h} - t'}{s} + \frac{s}{2} \ln \left(1 + \frac{(\tilde{h} - t')^2}{s^2} \right) \right. \right. \\ &\quad \left. \left. - \left(t' \arctan \frac{-t'}{s} + \frac{s}{2} \ln \left(1 + \frac{t'^2}{s^2} \right) \right) \right]_{t'=0}^h, 0 \right)^T. \end{aligned}$$

(Here, the second component $I_2^{h, \tilde{h}}$ of $I^{h, \tilde{h}}$ is zero by symmetry.) \square

REFERENCES

- [Bob00] S. Bobbio. *Electrodynamics of Materials: Forces, Stresses, and Energies in Solids and Fluids*. Academic Press, San Diego, 2000.
- [Bro66] W.F. Brown. *Magnetoelastic Interactions*. Springer-Verlag, Berlin, 1966.
- [Car01] C. Carstensen. *Wissenschaftliches Rechnen I. Lecture Notes*, 2001. Christian-Albrechts-Universität, Kiel.
- [DKMO06] A. DeSimone, R.V. Kohn, S. Müller, and F. Otto. Recent analytical developments in micromagnetics. In G. Bertotti and I. Mayergoyz, editors, *The Science of Hysteresis*, volume II, pages 269–383. Academic Press, 2006.
- [DPG96] A. DeSimone and P. Podio-Guidugli. On the Continuum Theory of Deformable Ferromagnetic Solids. *Arch. Ration. Mech. Anal.*, 136:201–233, 1996.
- [Eim06] T. Eimüller. Personal communication, Ruhr University of Bochum, 2006.
- [EM90] A.C. Eringen and G.A. Maugin. *Electrodynamics of continua*. Springer-Verlag, New York, 1990.
- [HS98] A. Hubert and R. Schäfer. *Magnetic domains. The analysis of magnetic microstructures*. Springer-Verlag, New York, 1998.
- [Jam02] R.D. James. Configurational Forces in Magnetism with Application to the Dynamics of a Small-Scale Ferromagnetic Shape Memory Cantilever. *Continuum Mech. Thermodyn.*, 14:55–86, 2002.

- [Mai99] M. Maischak. The Analytical Computation of the Galerkin Elements for the Laplace, Lamé and Helmholtz Equation in 2D-BEM. Technical Report ifam48, Institut für Angewandte Mathematik, Universität Hannover, 1999.
- [Mai00] M. Maischak. The Analytical Computation of the Galerkin Elements for the Laplace, Lamé and Helmholtz Equation in 3D-BEM. Technical Report ifam50, Institut für Angewandte Mathematik, Universität Hannover, 2000.
- [Pab06] S. Pabst. Analytische Berechnung und Untersuchung von magnetischen Kräften. Praktikumsbericht, Max Planck Institute for Mathematics in the Sciences, Leipzig, 2006.
- [PPS] N. Popović, D. Praetorius, and A. Schlömerkemper. Analysis and Numerical Simulation of Magnetic Forces between Rigid Polygonal Bodies. Part I: Analysis. Max Planck Institute for Mathematics in the Sciences, Leipzig, Preprint 63/2006, to appear in *Contin. Mech. Thermodyn.*
- [Pra03] D. Praetorius. *Analysis, Numerik und Simulation eines relaxierten Modellproblems zum Mikromagnetismus*. PhD thesis, Vienna University of Technology, Vienna, 2003.
- [Sch02] A. Schlömerkemper. *Magnetic forces in discrete and continuous systems*. PhD thesis, University of Leipzig, Leipzig, 2002.
- [Sch05] A. Schlömerkemper. Mathematical derivation of the continuum limit of the magnetic force between two parts of a rigid crystalline material. *Arch. Rational Mech. Anal.*, 176:227–269, 2005.
- [SS07] A. Schlömerkemper and B. Schmidt. Discrete-to-continuum limits of magnetic forces in dependence on the distance between bodies. Preprint, 2007.

BOSTON UNIVERSITY, DEPARTMENT OF MATHEMATICS AND STATISTICS AND CENTER FOR BIODYNAMICS, 111 CUMMINGTON STREET, BOSTON, MA 02215, U.S.A.

VIENNA UNIVERSITY OF TECHNOLOGY, INSTITUTE FOR ANALYSIS AND SCIENTIFIC COMPUTING, WIEDNER HAUPTSTRASSE 8-10, A-1040 VIENNA, AUSTRIA

CORRESPONDING AUTHOR. MAX PLANCK INSTITUTE FOR MATHEMATICS IN THE SCIENCES, INSELSTRASSE 22-26, D-04103 LEIPZIG, GERMANY, EMAIL: schloem@mis.mpg.de, TEL: +49-341-9959-547, FAX: +49-341-9959-633